energies

MDPI

Article

Probabilistic Modeling of Available Transfer Capability with Dynamic Transmission Reliability Margin for Renewable Energy Export and Integration

Uchenna Emmanuel Edeh [1], Tek Tjing Lie [1,*] and Md Apel Mahmud [2]

[1] Department of Electrical and Electronic Engineering, Auckland University of Technology, Auckland 1010, New Zealand; uchenna.edeh@autuni.ac.nz
[2] College of Science and Engineering, Flinders University, Adelaide, SA 5001, Australia; apel.mahmud@flinders.edu.au
* Correspondence: tek.lie@aut.ac.nz

Abstract

This paper develops a probabilistic Available Transfer Capability (ATC) framework that quantifies export headroom for renewables across transmission-distribution interfaces under time-varying uncertainty. Static transmission reliability margins can unnecessarily curtail exports. A dynamic transmission reliability margin (TRM) is embedded within ATC using rolling window statistics and adaptive confidence factor scheduling to release capacity in calm periods and tighten margins during volatile transitions. Uncertainty is modeled as net nodal power imbalance variability from load and renewable deviations, together with stochastic thermal limit fluctuations. Correlated multivariate scenarios are generated via Latin Hypercube Sampling with Iman-Conover correlation preservation and propagated through full AC power flow analysis. Validation on the IEEE 39-bus system and New Zealand's HVDC inter-island corridor recovers 93.31 MW of usable transfer capacity on the IEEE system relative to the pooled Monte Carlo P95 constant-margin baseline, with 78.11 MW attributable to rolling window volatility tracking and 15.20 MW to adaptive confidence factor scheduling, and 59.51 MW (+7.6%) on the New Zealand corridor relative to the corresponding pooled Monte Carlo P95 baseline, with the gain arising primarily from rolling window volatility tracking. Relative to a 95% one-sided reliability target, achieved coverage is 93.9% for IEEE and 91.8% for New Zealand, translating into increased export headroom and reduced curtailment.

Keywords: available transfer capability (ATC); transmission reliability margin (TRM); Latin Hypercube Sampling (LHS); rolling window uncertainty estimation; renewable energy integration; probabilistic power flow; distribution-connected renewable export; transmission–distribution interface

Academic Editor: Jesus C. Hernandez

Received: 11 March 2026
Revised: 6 April 2026
Accepted: 7 April 2026
Published: 10 April 2026

1. Introduction

1.1. Background and Motivation

The global push toward decarbonization has accelerated the integration of variable renewable energy sources (vRESs), particularly wind and photovoltaic generation, across both transmission and distribution networks [1]. As these distributed resources grow, renewable export increasingly depends on upstream transfer capability at the transmission–distribution interface. In renewable-rich systems, injections (load and renewable outputs) and effective transfer constraints (e.g., corridor thermal capability under changing operating

conditions) can be time-varying and non-stationary, meaning static reliability margins may over-reserve during calm periods—unnecessarily curtailing renewable export—or under-reserve during volatile transitions, compromising system security.

In this context, Available Transfer Capability (ATC) remains a critical operational metric that quantifies the additional power that can be reliably transferred without violating security constraints. According to the North American Electric Reliability Corporation (NERC), *ATC* is derived from total transfer capability (TTC) after subtracting existing commitments and reliability margins [2]. Mathematically, *ATC* is defined by Equation (1).

$$ATC = TTC - ETC - TRM - CBM \quad (1)$$

where *TTC* is total transfer capability, *ETC* is existing transmission commitments, *CBM* is capacity benefit margin, and *TRM* is transmission reliability margin.

1.2. Limitations of Existing Probabilistic ATC Approaches

Existing probabilistic ATC methods include Monte Carlo simulation, polynomial chaos expansion, point estimate methods, and bootstrap-based approaches. MCS is flexible but computationally intensive; surrogate and reduced-order methods improve efficiency but can degrade in high-dimensional settings; and resampling-based methods remain sensitive to data representativeness. These approaches generally focus on probabilistic TTC/ATC estimation itself, rather than on dynamic time-varying TRM adjustment within ATC. To address the limitations of deterministic assessment, probabilistic approaches to ATC calculation have been widely investigated, including Monte Carlo and related uncertainty propagation techniques that estimate transfer limit distributions under uncertain operating conditions [3], as well as broader ATC calculation method surveys that document the evolution of analytical, simulation-based, and scenario-driven formulations [4]. Despite these advances, existing probabilistic ATC frameworks still exhibit several key limitations. Firstly, many approaches primarily model injection-side uncertainty while neglecting variability in transmission constraints themselves. For example, Sun et al. [5] used a statistically equivalent low-rank approximation to estimate probabilistic ATC under wind and load uncertainty but did not model constraint-side (thermal limit) variability or address time-varying uncertainty dynamics. Reyad et al. [6] similarly provided a probabilistic ATC framework that incorporates load and wind uncertainty, but its uncertainty modeling remains time-invariant and does not support online adaptive margin updating. Secondly, uncertainty characterization is often based on stationary or historically derived scenario representations that do not fully capture evolving forecast errors and regime changes. Recent data-driven ATC approaches have improved uncertainty representation through multiarea scenario generation and probabilistic congestion forecasting [7,8], but they still do not embed an explicitly adaptive TRM mechanism that updates reliability margins online in response to non-stationary operating conditions. Thirdly, chance-constrained and stochastic optimization-based formulations increasingly embed ATC assessment within OPF/SCOPF-type frameworks to enforce feasibility under uncertainty [5]; however, their scenario handling, reformulation steps, or repeated simulation burden often make them more suitable for planning or offline analysis than near-real-time operational deployment. Fourthly, most probabilistic ATC studies are formulated from a bulk transmission perspective, with limited interpretation in terms of distribution-connected renewable export headroom and curtailment at the transmission–distribution interface.

1.3. Research Gap in TRM Practice

TRM is a key component of ATC calculation, intended to account for uncertainties in system conditions and transfer capability assessments [9,10]. In current industry prac-

tice, TRM is often implemented as a fixed MW value or a fixed percentage of TTC, and probabilistic TRM is commonly applied as a time-invariant quantile-based margin (i.e., fixed confidence factor K or z-score) estimated from historical snapshots and held constant over long intervals. In current practice, TRM magnitudes vary across TSOs and transfer paths. For example, BC Hydro reports a fixed TRM of 50 MW on the BC Hydro–USA tie-line, which is broadly consistent with approximately 1.9–2.8% of the mean TTC values reported for representative hourly, daily, and weekly cases in its published assessment. These fixed-margin implementations, whether expressed in MW or as a percentage of TTC/NTC, do not adapt to time-varying uncertainty and operating conditions [9], potentially yielding overly conservative margins that restrict transmission utilization and curtail renewable export, or insufficient margins that expose the system to elevated reliability risk during high-uncertainty intervals. Accordingly, there is a need for probabilistic ATC frameworks in which reliability margins are updated at operational timescales based on observed uncertainty dynamics rather than imposed as static safety buffers.

Motivated by these limitations, this study targets the following gaps in the literature:

- Limited real-time adaptivity: Most probabilistic ATC/TRM methods (e.g., [3,6,11]) rely on stationary uncertainty representations with fixed probabilistic parameters, and do not incorporate online adaptation to evolving forecast errors or regime changes.
- Incomplete integration of multiple concurrent uncertainty sources: Existing studies (e.g., [12]) typically model injection-side uncertainty only, while constraint-side variability (e.g., thermal limit fluctuations) is treated separately rather than integrated within a unified ATC–TRM interaction framework [13].
- Lack of validated dynamic ATC/TRM frameworks: Earlier rolling or adaptive TRM formulations [14] demonstrated dynamic margin estimation on benchmark test systems, but were not extended to a full probabilistic ATC framework with cross-system validation using real operational data.
- Computational burden that can restrict online applicability: Chance-constrained and stochastic OPF-based approaches provide rigorous uncertainty-aware formulations, but high-dimensional uncertainty, scenario growth, and multi-stage complexity can make real-time deployment challenging and often favor day-ahead, planning, or other offline applications.

Although our prior work examined rolling window TRM estimation under time-varying uncertainty, the present study goes beyond dynamic margin estimation alone. Specifically, this paper embeds dynamic TRM within a full probabilistic ATC framework that jointly models injection-side and constraint-side uncertainty, preserves dependence through LHS with Iman–Conover rank correlation control, propagates uncertainty through AC power flow-based TTC assessment, and interprets recovered transfer capability as renewable export headroom at the transmission–distribution interface. In this sense, the manuscript extends rolling window TRM from a margin estimation concept into an operational probabilistic ATC framework for renewable-rich networks.

To address the above gaps, this paper proposes a probabilistic ATC framework in which dynamic TRM is embedded directly within ATC assessment and updated in response to time-varying uncertainty.

The main contributions are summarized as follows:

1. Dynamic TRM embedded in ATC: A rolling window TRM is integrated into ATC calculation so that reliability margins can track time-varying uncertainty at operational timescales.
2. Multi-source uncertainty representation: The framework jointly models injection-side uncertainty (load, wind, and solar forecast errors) and constraint-side uncertainty (stochastic thermal limit variability) within a unified probabilistic ATC–TRM formulation.

3. Correlation-preserving scenario generation: Dependent multivariate scenarios are generated using Latin Hypercube Sampling (LHS) with Iman–Conover correlation preservation and propagated through full AC power flow constraints.
4. Validation and operational interpretation: The framework is evaluated on the IEEE 39-bus benchmark and New Zealand HVDC inter-island corridor data and recovered transfer capacity is interpreted as export headroom for renewables at the transmission–distribution interface, linking dynamic margining to curtailment reduction.

The remainder of this paper is organized as follows: Section 2 reviews related work on probabilistic ATC and TRM estimation. Section 3 presents the proposed formulation. Section 4 describes the case studies and data. Section 5 reports the results. Section 6 discusses implications for renewable export at the transmission–distribution interface. Section 7 concludes the paper.

2. Related Works

2.1. Deterministic and Static ATC Assessment

ATC has conventionally been assessed using deterministic frameworks based on fixed operating conditions and predefined security margins. NERC defines ATC as the remaining transfer capability after accounting for existing commitments and reliability margins (including TRM and CBM), yielding an operationally simple metric for planning and scheduling.

However, deterministic ATC implicitly assumes time-invariant uncertainty and limited variability in system conditions. In renewable-rich systems, stochastic injections and evolving operating states violate these assumptions, so static margining can either over-reserve during calm periods (curtailing exports) or under-reserve during volatile intervals (increasing risk), leading to inefficient transfer utilization and reduced renewable export headroom (Figure 1).

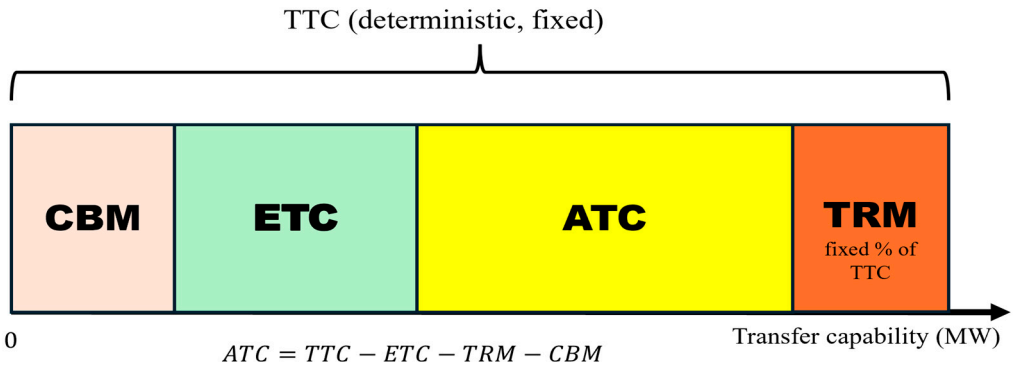

Figure 1. Deterministic ATC formulation with fixed TRM (TRM expressed as a percentage of TTC).

2.2. Probabilistic ATC Assessment Under Renewable Uncertainty

To overcome limitations of deterministic ATC evaluation, probabilistic ATC methods explicitly model uncertainty in system inputs and propagate it through power flow constraints to obtain ATC distributions. Monte Carlo simulation (MCS)-based probabilistic power flow has been widely used to represent load and renewable variability, but typically requires many samples for convergence, resulting in high computational cost that limits time-sensitive operational use [15]. To improve efficiency, sampling and scenario-based approaches such as LHS, importance sampling, and scenario reduction have been adopted [16]. Surrogate models have also been introduced to accelerate evaluation; for instance, ref. [11] used a statistically equivalent low-rank approximation to estimate probabilistic ATC under wind and load uncertainty with improved tractability. Chronological

extensions (e.g., sequential MCS) further capture time-dependent uncertainty from load fluctuations and component availability, highlighting that ATC can vary over time under stochastic conditions.

More recently, data-driven scenario generation methods, including machine learning and generative models, have been explored to improve scenario fidelity in high-dimensional uncertainty settings. Chance-constrained and stochastic optimization-based formulations have also embedded ATC within security-constrained OPF frameworks to enforce feasibility under uncertainty, although their computational burden often limits their application to planning or offline studies. Overall, most probabilistic ATC studies focus primarily on injection-side uncertainty, while variability in transmission constraints is often treated separately rather than integrated within a unified ATC–TRM interaction framework. Moreover, many methods rely on stationary uncertainty assumptions or offline calibration, limiting responsiveness to non-stationary renewable-driven uncertainty.

Notably, earlier probabilistic ATC models typically employ independent sampling, such as standard MCS or LHS without explicit correlation control, which can underestimate tail risk when forecast errors are spatially correlated. This effect is demonstrated quantitatively in Section 5.2.2 of this paper, where neglecting dependence shifts the 5th-percentile TTC by 23.35 MW. Furthermore, none of the above methods integrates a dynamically adjusted TRM; instead, the reliability margin is either fixed a priori or derived as a static quantile from pooled Monte Carlo output, thereby foregoing potential transfer capacity recovery during low-volatility intervals.

Finally, existing work rarely interprets probabilistic ATC outcomes in terms of export headroom constraints for renewables interconnected at the transmission–distribution interface. Figure 2 illustrates the proposed probabilistic ATC formulation with dynamic TRM, contrasting the adaptive margin structure with the fixed allocation shown in Figure 1.

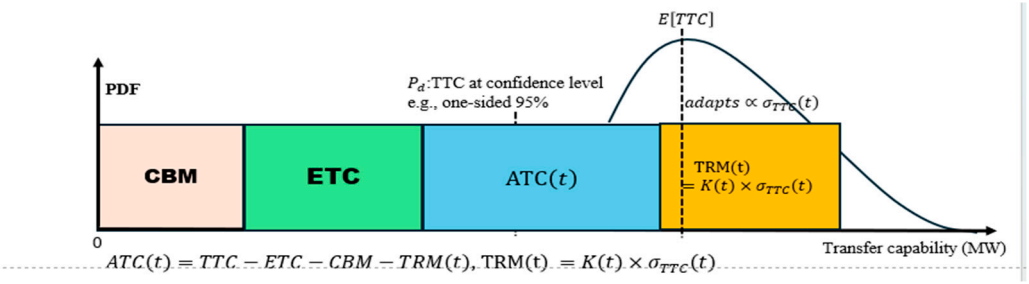

Figure 2. Probabilistic ATC formulation with dynamic TRM.

2.3. Robust and Distributionally Robust ATC Formulations

In parallel, robust and distributionally robust optimization frameworks have been introduced to mitigate uncertainty distribution ambiguity and structural model mismatch. These methods seek to guarantee feasibility under worst-case or ambiguity set-defined uncertainty realizations, thereby enhancing reliability when probabilistic information is limited. Distributionally robust formulations, in particular, provide a middle ground between stochastic and robust optimization by optimizing against a family of plausible probability distributions rather than assuming a single known distribution.

Despite their strong theoretical guarantees, robust formulations can yield conservative ATC estimates and typically rely on static uncertainty sets that do not reflect time-varying uncertainty dynamics in renewable-rich systems. Moreover, their computational complexity and dependence on offline solution procedures often limit applicability in near-real-time operational settings where rapid ATC updates are required [17].

2.4. Transmission Reliability Margin Modeling

TRM is a critical component of ATC determination, intended to cover uncertainty in system conditions, measurement/forecast errors, and modeling approximations. Existing TRM approaches include fixed-margin rules (MW or percentage), probabilistic margins derived from historical deviations (e.g., quantile-/z-score-based), and sensitivity-based formulations that relate uncertainty sources to transfer limits. However, with increasing renewable penetration, uncertainty becomes time-varying and state-dependent, so static or offline-calibrated TRM implementations can be overly conservative in calm periods or insufficient during volatile transitions.

In parallel, constraint-side uncertainty (e.g., variability in effective thermal limits) has been studied, but it is often treated as a standalone adjustment rather than integrated within a unified probabilistic ATC formulation in which TRM is dynamically updated. Moreover, many probabilistic ATC/TRM methods remain computationally intensive, limiting near-real-time deployment. These observations motivate probabilistic ATC frameworks that embed TRM as a dynamic, uncertainty-driven margin, jointly capturing injection-side and constraint-side uncertainty while updating reliability margins at operational timescales [13].

3. Proposed Methodology

ATC represents the remaining transfer capability after accounting for existing commitments and reliability margins. In the NERC framework, ATC is defined as in (1) [18]. The proposed framework proceeds in three integrated stages: (i) marginal uncertainty distributions for load, wind, solar, and thermal limit variability are characterized; (ii) correlated multivariate scenarios are generated via LHS with Iman–Conover rank correlation control to preserve inter-variable dependence; and (iii) these scenarios are propagated through full AC power flow to obtain TTC distributions, from which rolling window statistics and adaptive confidence factor scheduling produce time-varying TRM and ATC. This pipeline ensures that marginal uncertainty, spatial correlation, and nonlinear network physics are jointly captured.

In this work, ETC and CBM are treated as deterministic parameters, while uncertainty is captured through the probabilistic characterization of TTC and the dynamic estimation of TRM under time-varying conditions.

3.1. AC Power Flow Formulation

Although Power Transfer Distribution Factor (PTDF)-based DC formulations are computationally efficient, they neglect reactive power, voltage variations, and losses; therefore, this study employs full AC power flow to ensure reliable ATC and dynamic TRM estimation under renewable-rich operating conditions.

For each bus $\boldsymbol{i}$, the steady-state real and reactive power balance equations are given by Equations (2) and (3).

$$\boldsymbol{P_i} = \boldsymbol{V_i}\sum_{j=1}^{N} \boldsymbol{V_j}\left(\boldsymbol{G_{ij}cos\theta_{ij}} + \boldsymbol{B_{ij}sin\theta_{ij}}\right) \quad (2)$$

$$\boldsymbol{Q_i} = \boldsymbol{V_i}\sum_{j=1}^{N} \boldsymbol{V_j}\left(\boldsymbol{G_{ij}sin\theta_{ij}} - \boldsymbol{B_{ij}cos\theta_{ij}}\right) \quad (3)$$

where P_i and Q_i are the real and reactive power injections at bus i, V_i and V_j are the voltage magnitudes at buses i and j, $\theta_{ij} = \theta_i - \theta_j$ is the voltage angle difference between buses i and j; and G_{ij} and B_{ij} are the real and imaginary parts of the bus admittance matrix. The summation is taken over all buses j = 1, ……, N in the network. The resulting nonlinear algebraic equations are solved using the Newton–Raphson method with a convergence tolerance of 10^{-6} p.u. for both real and reactive power mismatches, implemented in

MATPOWER [19]. Non-converged scenarios, if any, are excluded from the TTC distribution to prevent biased estimates.

3.2. Branch Flow and Thermal Constraints

The apparent power on transmission line l is computed from the AC power flow solution shown in Equation (4).

$$S_l = \sqrt{{P_l}^2 + {Q_l}^2} \tag{4}$$

where P_l and Q_l represent the transmission lines' real and reactive power flows, respectively. Line loading is assessed against thermal limits using Equation (5).

$$\eta_l = \frac{S_l}{{S_l}^{max}} \times 100\% \tag{5}$$

where S_l is the apparent power flow on line l, and $S_l^{\max}$ is the MVA thermal rating of line l.

3.3. Simulation-Based TTC Determination

The TTC between an exporting area (Area 1) and an importing area (Area 2) is evaluated through simulation-based assessment. The inter-area transfer is defined by Equation (6).

$$T_{1\to 2} = \sum_{l\in L_{tie}} {P_l}^{dir} \tag{6}$$

where $\mathcal{L}_{tie}$ denotes the set of tie-lines connecting the two areas and P_l^{dir} is the real power flow on tie-line l measured positive from Area 1 to Area 2. The TTC is determined as the maximum transferable power such that all thermal limits are respected under all credible contingencies as shown by Equation (7).

$$TTC = max\{T_{1\to 2} : \eta_l \leq 100\%, \forall l \in L, \forall c \in C\} \tag{7}$$

subject to branch thermal constraints (Equation (5)) and bus voltage operational limits for the intact (N-0) network topology. While Equation (7) can be extended to include post-contingency topologies by iterating over a contingency set C, the present implementation evaluates TTC under the intact network configuration only. Stochastic thermal limit perturbations (Equation (19)) implicitly capture rating variability effects, but do not substitute for explicit N-1 contingency screening. For systems where N-1 security is binding, the framework can be extended straightforwardly by evaluating TTC for each uncertainty scenario under each post-contingency topology, at a computational cost that scales with $\mid C \mid \times N$. Accordingly, TTC in the present study is determined by the active branch thermal and bus voltage constraints under the intact-network AC power flow solution, with the binding constraint identified endogenously.

3.4. Uncertainty Characterization

Short-term uncertainty in renewable-rich power systems arises from stochastic variations in load demand, wind generation, solar PV generation, and network constraints. These uncertainties directly affect nodal power injections and propagate through the transmission network, inducing variability in line flows, transfer capability, and reliability margins. Accordingly, two complementary classes of uncertainty are modeled in this study: (i) injection-side uncertainty captured through net nodal power imbalance resulting from load–wind–solar variability, and (ii) constraint-side uncertainty represented through stochastic variability in transmission line thermal capacity.

3.4.1. Load Demand Uncertainty Modeling

Over short forecasting horizons, load forecast errors are commonly approximated as near-Gaussian due to aggregation across numerous independent consumption behaviors. Accordingly, load demand uncertainty is modeled using a normal distribution as shown in Equation (8).

$$f_L(P_L) = \frac{1}{\sigma_L\sqrt{2\pi}}\, exp\left(-\frac{(P_L-\mu_L)^2}{2{\sigma_L}^2}\right) \tag{8}$$

where P_L is the actual load, μ_L is the expected (forecast) load, σ_L is the forecast error standard deviation, and $f_L(P_L)$ is the probability density function (pdf) of P_L. Consistent with operational studies, σ_L is selected as a percentage of the forecast load to reflect typical short-term forecasting accuracy. This probabilistic representation captures stochastic load deviations while maintaining computational efficiency for scenario generation.

3.4.2. Wind Speed and Wind Power Uncertainty Modeling

Wind power uncertainty arises from the variability in and intermittency of atmospheric conditions. In this work, wind speed is modeled probabilistically and mapped to electrical power output using a turbine power curve. Wind speed v is modeled using a two-parameter Weibull distribution given in Equation (9).

$$f_v(v) = \frac{k}{c}\left(\frac{v}{c}\right)^{k-1}\exp\left[-\left(\frac{v}{c}\right)^{k}\right] \tag{9}$$

where k and c denote the shape and scale parameters, respectively. For this study, $k = 2$ and $c = 8$ m/s are adopted, representing typical onshore wind characteristics. Wind speed realizations are converted to wind power using the standard piecewise turbine power curve represented by Equation (10).

$$P_{\text{wind}}(v) = \begin{cases} 0, & v < v_{\text{ci}} \\ P_r\,\frac{v-v_{\text{ci}}}{v_r-v_{\text{ci}}}, & v_{\text{ci}} \le v < v_r \\ P_r, & v_r \le v < v_{\text{co}} \\ 0, & v \ge v_{\text{co}} \end{cases} \tag{10}$$

where v_{ci}, v_r, and v_{co} are the cut-in, rated, and cut-out wind speeds, respectively, and P_r is the rated wind power.

3.4.3. Solar Irradiance and Solar PV Power Uncertainty Modeling

Solar PV generation uncertainty arises from stochastic variations in solar irradiance driven by cloud cover, atmospheric conditions, and diurnal solar patterns. Because solar output is physically bounded, short-term irradiance uncertainty is modeled using a Beta distribution [20] shown in Equation (11). Irradiance is first normalized by its maximum physically admissible value [21].

$$\widetilde{G}(t) = \frac{G(t)}{G_{\text{max}}}, \quad 0 \le \widetilde{G}(t) \le 1 \tag{11}$$

The normalized irradiance $\widetilde{G}(t)$ is then modeled as Equation (12)

$$\widetilde{G}(t) \sim \text{Beta}(\alpha,\ \beta) \tag{12}$$

where α and β are shape parameters that reflect site-specific solar variability. In this study, $\alpha = 2$ and $\beta = 5$ are adopted following established practice [22], yielding a right-skewed distribution with mean $\mu = \alpha/(\alpha + \beta) \approx 0.29$.

Solar irradiance realizations are converted to photovoltaic power output using a linearized conversion model shown in Equation (13).

$$P_{\text{solar}}(t) = P_r \, \widetilde{G}(t) \tag{13}$$

where P_r denotes the rated capacity of the PV installation. This approximation is computationally efficient and suitable for transmission-level probabilistic analysis.

3.4.4. Net Load and Net Nodal Power Imbalance Uncertainty

To combine the effects of load, wind, and solar uncertainty in a network-relevant form, the net load at time (t) is defined by Equation (14).

$$P_{\text{net}}(t) = P_{\text{load}}(t) - P_{\text{wind}}(t) - P_{\text{solar}}(t) \tag{14}$$

These net load imbalances propagate through the transmission network, inducing uncertainty in line flows and inter-area transfer capability and thereby constituting a primary driver of transmission reliability margin requirements. The net nodal power imbalance at bus i is defined by Equation (15).

$$\xi_i^P(t) = P_i^{actual}(t) - P_i^{forecast}(t) \tag{15}$$

where $\xi_i^P(t)$ denotes the deviation between actual and forecast net power injection at bus i.

Using a rolling window of length W, the sample mean and standard deviation of the nodal imbalance are computed using Equations (16) and (17).

$$\widehat{\mu}_i = \frac{1}{W}\sum_{k=1}^{W} \xi_i^p(t-k) \tag{16}$$

$$\widehat{\sigma}_i = \sqrt{\frac{1}{W-1}\sum_{k=1}^{W}\left(\xi_i^p(t-k) - \widehat{\mu}_i\right)^2} \tag{17}$$

These nodal-level rolling statistics are used to characterize spatially distributed forecast uncertainty and its propagation through the transmission network. They are conceptually distinct from the system-level rolling statistics introduced in Section 3.8, which operate on aggregated forecast errors to support adaptive TRM estimation.

Spatial dependence among nodal forecast errors is modeled using Pearson correlation, consistent with established probabilistic power system studies. Although Pearson correlation captures only linear dependence, it is sufficient for characterizing second-order uncertainty over short horizons, while nonlinear system interactions are explicitly addressed through AC power flow analysis. The correlation coefficient between buses i and j is given by Equation (18).

$$R_{ij} = \frac{\sum_{k=1}^{W}\left(\xi_i^p(t-k) - \widehat{\mu}_i\right)\left(\xi_j^p(t-k) - \widehat{\mu}_j\right)}{\left[(W-1)\sigma_i\sigma_j\right]} \tag{18}$$

The resulting correlation structure enables realistic representation of spatially dependent uncertainty while preserving computational tractability for real-time ATC assessment.

3.4.5. Transmission Line Thermal Capacity Uncertainty

Transmission constraints are governed by thermal limits, network topology, and contingency requirements. In this study, uncertainty is modeled only through variability in transmission line thermal ratings, while topology and contingency conditions are enforced deterministically via AC power flow analysis [23]. The effective thermal capacity of line l at time t is given by Equation (19).

$$S_l^{eff}(t) = S_l^{nom}(1 + \varepsilon_l(t)) \tag{19}$$

where S_l^{nom} is the nominal (static) thermal rating and $\varepsilon_l(t)$ captures short-term rating variability due to environmental effects (e.g., ambient temperature and wind cooling) and modeling uncertainty. This is a stochastic approximation of short-term thermal limit variability and does not explicitly implement dynamic line rating.

The random variable $\varepsilon_\ell(t)$ is assumed to follow a truncated normal distribution as expressed in Equation (20).

$$\varepsilon_{l\sim} N_{trunc}\left(0, {\sigma_\varepsilon}^2, -\varepsilon_{max}, +\varepsilon_{max}\right) \tag{20}$$

This ensures that effective line ratings remain within physically admissible bounds. Typically, values of the standard deviation σ_ε are reported in the range of 2–5% of the nominal line rating, reflecting short-term uncertainty due to ambient temperature variation, wind cooling effects, and modeling inaccuracies [24].

3.5. Scenario Generation via Latin Hypercube Sampling

To efficiently propagate multivariate uncertainty through the nonlinear AC power flow model, LHS with Iman–Conover rank correlation control is employed [25]. LHS is preferred over alternative sampling strategies for several reasons. Quasi-Monte Carlo (QMC) sequences, such as Sobol and Halton, provide excellent space-filling properties in low-dimensional settings, but their practical advantage can diminish in moderate-to-high dimensions, and they do not natively accommodate rank correlation control. Sparse-grid quadrature, such as Gauss–Hermite rules, offers high accuracy for smooth response surfaces, but suffers from the curse of dimensionality, since the number of grid points grows rapidly with the number of uncertain variables, rendering it impractical for the 30+ input dimensions considered in this study. In contrast, LHS provides stratified coverage of each marginal distribution under a fixed sample budget, is directly compatible with the Iman–Conover rank reordering technique for enforcing arbitrary dependence structures and typically achieves lower estimator variance than standard Monte Carlo sampling for the same number of scenarios. In this study, M = 1000 LHS scenarios are generated. This sample size is justified by the convergence analysis in Section 5.1, which demonstrates that the mean TTC stabilizes within 0.13% of the N = 10,000 MCS reference, with 5th-percentile accuracy within 1.56%.

This approach preserves prescribed marginal distributions while enforcing a target correlation structure among uncertain variables. Independent LHS samples are first generated for each uncertain parameter. For M scenarios, the marginal samples are generated as shown in Equation (21).

$$u_i^{(m)} = \frac{\pi_i(m) - U(0,1)}{M}, \quad m = 1, 2 \ldots, M \tag{21}$$

where $\pi_i(m)$ is a random permutation of $\{1, 2 \ldots, M\}$ for the i-th uncertain variable.

These marginal samples are transformed to the target marginal distributions using inverse cumulative distribution functions (CDFs) as shown in Equation (22).

$$\xi_i^m = {F_i}^{-1}(u_i^m) \tag{22}$$

where ${F_i}^{-1}(.)$ represents the inverse CDF (quantile function) of the i-th uncertain variable.

To impose correlation among uncertainties, the Iman–Conover rank correlation method is applied. An auxiliary set of correlated normal samples is generated using the Cholesky decomposition of the target correlation matrix C. The rank ordering of the independent LHS samples is then rearranged to match the rank ordering of the correlated normal samples, thereby inducing the desired correlation structure while preserving the marginal distributions.

This rank-based approach avoids assumptions of joint normality and provides an efficient and robust means of modeling correlated uncertainty suitable for near-real-time ATC assessment.

3.6. Baseline Models for Forecast Deviation

A persistence forecasting model is adopted as a baseline, in which the forecasted value at a future horizon h is assumed equal to a previously observed realization of the same process. In its general form, the persistence model is expressed in Equation (23).

$$\widehat{\xi}_i(t + h) = \xi_i(t) \tag{23}$$

where $\xi_i(t)$ denotes the observed value of the stochastic variable i at time t, and h represents the forecast horizon.

For load demand forecasting, a diurnal persistence assumption is employed to reflect the strong daily periodicity of power consumption. Accordingly, the forecasted load at time t is taken as the actual load observed 24 h earlier, given by Equation (24).

$$P_{forecast,t} = P_{actual,\ t-24\text{h}} \tag{24}$$

This formulation provides a simple yet robust benchmark for generating short-term load forecast errors used in the probabilistic uncertainty analysis.

In addition to persistence, a moving-average baseline model is considered to provide a smooth reference forecast. The moving-average forecast is expressed by Equation (25).

$$\widehat{\xi}_i(t+h) = \sum_{k=0}^{k-1} w_k \xi_i(t-k) \tag{25}$$

where K represents the moving-average window length and w_k are non-negative weighting coefficients satisfying $\sum_{k=0}^{K-1} w_k = 1$. Unless otherwise stated, uniform weights $w_k = 1/K$ are adopted.

Residuals obtained from these baseline models are subsequently used to estimate the forecast error variance required for the probabilistic modeling of load uncertainty.

3.7. Rolling Window Statistical Framework

To characterize time-varying forecast uncertainty under non-stationary operating conditions, a rolling window statistical framework is adopted [14,26]. A sliding window of length W retains the most recent forecast error samples $\{e_{t-W+1}, \ldots, e_t\}$, where e_t represents the aggregated forecast error associated with net load or inter-area transfer at

time t. Within each window, the rolling mean μ_t and standard deviation σ_t are computed using Equations (26) and (27).

$$\mu_t = \frac{1}{W}\sum_{i=t-W+1}^{t} e_i \tag{26}$$

$$\sigma_t = \sqrt{\frac{1}{W-1}\sum_{i=t-W+1}^{t}(e_i - \mu_t)^2} \tag{27}$$

The window-length choice reflects a trade-off between statistical stability and responsiveness. The window range $[W_{\min}, W_{\max}] = [15, 60]$ min is selected to span operationally relevant timescales between automatic generation control (AGC, ~4–10 min) and hourly scheduling (~60 min). Shorter windows (<15 min) contain too few samples for reliable variance estimation: at 5 min resolution, $W = 15$ min yields only 3 samples, which is the practical minimum for computing a standard deviation. Longer windows (m) smooth over intra-hour volatility transitions, increasing tracking lag and introducing downward bias in σ_t during volatile intervals, which would undersize TRM precisely when protection is most needed. This bias–responsiveness trade-off is quantified in Section 5.3.2: the 15 min window achieves 73.6% tracking accuracy but 31.6% estimation noise, while the 60 min window reduces noise to 28.4% but degrades tracking to 50.2% with a 9-step response lag. The 30 min baseline therefore provides the best practical compromise for the 5 min dispatch resolution adopted.

This rolling window mechanism enables continuous tracking of short-term volatility with computational efficiency suitable for near-real-time ATC assessment. In this study, e_t corresponds to the net load forecast error (capturing combined load, wind, and solar deviations), while transmission constraint uncertainty is treated separately via stochastic line thermal limits (Section 3.5). Unlike the nodal-level rolling statistics used for spatial uncertainty characterization, the statistics here operate on system-level aggregated errors and are used exclusively for adaptive TRM estimation. Figure 3 illustrates the complete adaptive rolling window TRM estimation pipeline, showing how the sliding window produces time-varying statistics (panel (a)) that feed into K(t) scheduling and dynamic TRM computation (panel (b)).

3.8. Dynamic Confidence Factor

Conventional probabilistic TRM formulations often assume forecast errors are stationary and approximately Gaussian, motivating a fixed confidence factor K (e.g., 95% one sided) in margin determination. In renewable-rich systems, forecast errors are frequently non-stationary and intermittent, so a fixed K can be either overly conservative in calm periods or insufficient during volatile transitions. To address this, a dynamic confidence factor $K(t)$ is defined by Equation (28) [14].

$$K(t) = K_{base} \times \left[1 + \beta\left(\frac{\sigma_t - \sigma_{ref}}{\sigma_{ref}}\right)\right] \tag{28}$$

For operationally realistic values, and to ensure physically admissible margins, the scheduled confidence factor is bounded within $[K_{min}, K_{max}]$ as shown in Equation (29).

$$K(t) = \max(K_{min}, min(K_{max}, K(t))) \tag{29}$$

where $K(t)$ is the time-varying confidence factor, K_{base} is the baseline Gaussian confidence level (95%), σ_{ref} is a reference standard deviation from historical data, σ_t is the rolling standard deviation at time t, and β is an adaptive scaling coefficient. The bounds $[K_{\min}, K_{\max}] = [1.10, 2.50]$ are selected to satisfy two operational objectives.

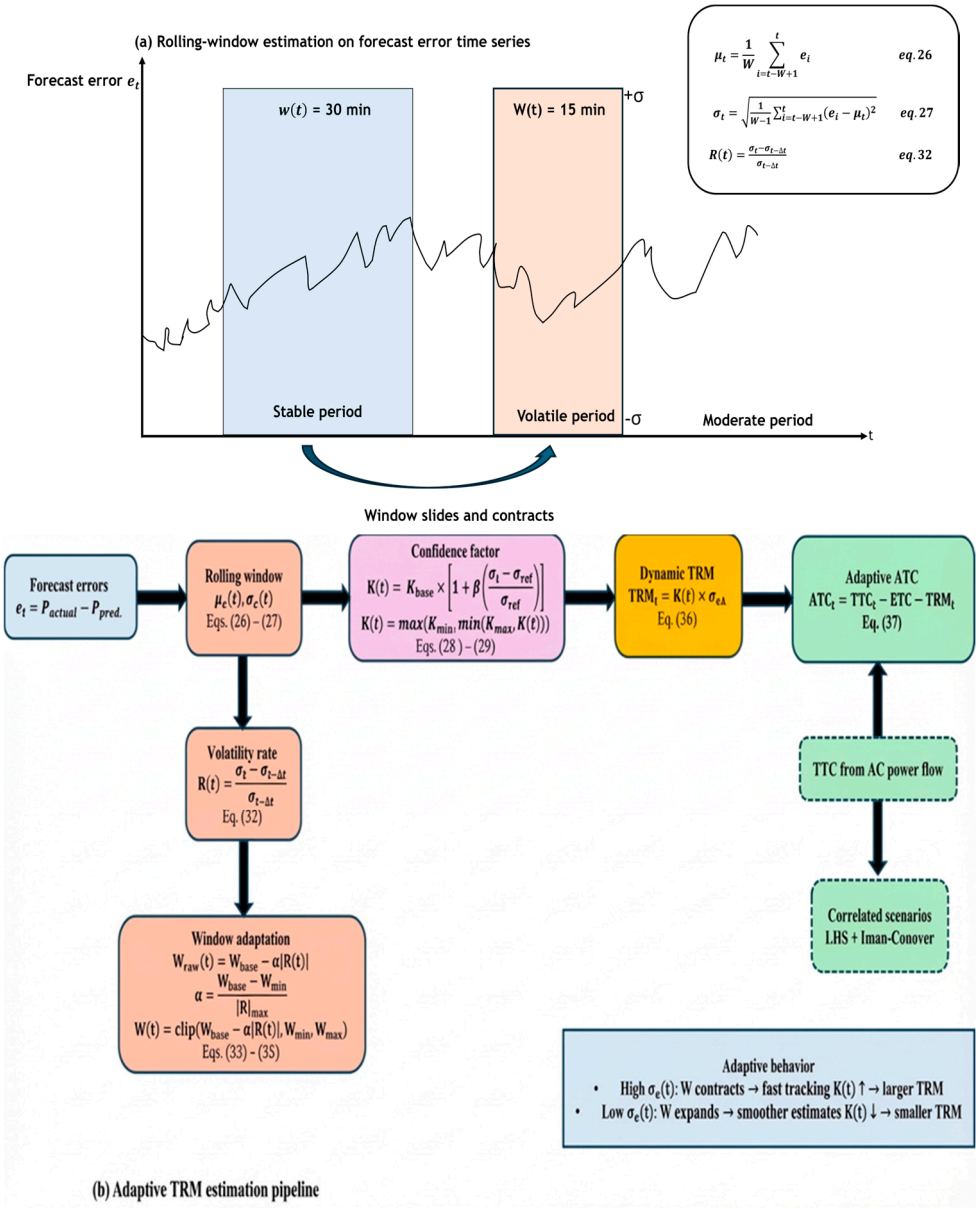

Figure 3. Schematic of the adaptive rolling window TRM estimation framework. (**a**) Sliding window expands in stable periods and contracts during volatile transitions, producing time-varying μ_t, $\sigma_{\mathrm{TTC}}(t)$, and $r(t)$. (**b**) Rolling estimates schedule $K(t)$ and compute dynamic TRM, with $W(t)$ updated from $r(t)$.

Firstly, $K_{\min} = 1.10$ ensures that, even under very stable conditions, TRM retains a minimum margin roughly equivalent to a one-sided Gaussian 86th-percentile level, thereby preventing the reliability margin from collapsing during low-volatility periods. Secondly, $K_{\max} = 2.50$ caps the margin at approximately the one-sided Gaussian 99.4th-percentile level, limiting excessive conservatism during short-lived volatility spikes that may not reflect sustained system stress. The frequency and effect of bound saturation are examined in Section 5.4.1.

The dependence of $K(t)$ on the normalized volatility ratio $\frac{\sigma_t - \sigma_{\mathrm{ref}}}{\sigma_{\mathrm{ref}}}$ is adopted as a first-order volatility scaling rule rather than a claim of universal optimality. The linear form is chosen for three practical reasons: monotonicity, interpretability, and low computational overhead for near-real-time implementation. In operational terms, elevated rolling uncertainty should lead to proportionally larger reliability margins, while calmer intervals should permit margin contraction. This approximation is appropriate when the normalized volatil-

ity deviation remains moderate, which is consistent with the operating regimes observed in the case studies. Moreover, the bounded formulation in Equation (29), through saturation at $K_{\min}$ and $K_{\max}$, limits the impact of higher-order nonlinear behavior in extreme conditions. While nonparametric quantile recalibration is an attractive alternative in principle, it would require repeated estimation of tail percentiles from short rolling samples, which is statistically unstable for the window sizes used here; for example, a 15 min window at 5 min resolution yields only three samples, far too few for reliable percentile estimation. The adequacy of the adopted mapping is therefore assessed empirically through achieved coverage and transfer capacity recovery rather than assumed from theoretical Gaussian optimality alone.

This formulation expands TRM under elevated volatility and contracts it during stable conditions, improving responsiveness without undue conservatism.

Scaling Coefficient β

The scaling coefficient β quantifies the relative contribution of renewable generation variability to overall net load uncertainty and is defined empirically by (30). The quadratic (root-sum-of-squares) combination of σ_{wind} and σ_{solar} follows from the assumption of approximate independence between wind and solar forecast errors, an assumption that is empirically consistent with the typically weak cross-correlation between wind speed and solar irradiance at operational timescales [27]. Under independence, the variance in the combined renewable forecast error is $\sigma_{wind}^2 + \sigma_{solar}^2$, and the corresponding standard deviation of the aggregated renewable contribution is $\sqrt{\sigma_{wind}^2 + \sigma_{solar}^2}$, which yields the form used in Equation (30).

$$\beta = \frac{\sqrt{{\sigma_{wind}}^2 + {\sigma_{solar}}^2}}{\sigma_{netload}} \tag{30}$$

where σ_{wind} and σ_{solar} denote the standard deviations of wind and solar power forecast errors, respectively, and $\sigma_{netload}$ represents the standard deviation of the combined net load forecast error, computed from load, wind, and solar forecast error components.

Transmission constraint uncertainty (σ_ε) is intentionally excluded from β because: (i) β is designed to capture the sensitivity of net load-driven TTC variability to renewable forecast errors, whereas thermal rating variability acts through a different physical mechanism, namely ambient condition effects on conductor capacity; and (ii) the variance decomposition in Section 5.2.1 shows that thermal rating uncertainty contributes negligibly to total TTC variance in the operating regime studied, so its inclusion would not materially affect β. A sensitivity analysis of β on TRM and ATC performance is reported in Section 5.4.4.

3.9. Window Size Sensitivity Analysis and Adaptive Sizing

To select an appropriate baseline window for rolling uncertainty estimation, fixed window lengths of 15, 30, and 60 min are evaluated to reflect typical operational timescales. For each candidate window length W, the rolling root-mean-square error (RMSE) is computed using Equation (31).

$$\mathrm{RMSE_t}(W) = \sqrt{\frac{1}{W}\sum_{i=t-W+1}^{t}\left(P_{forecast,\,i} - P_{actual,\,i}\right)^2} \tag{31}$$

which captures the trade-off between responsiveness and estimation noise. Based on RMSE trends and volatility tracking performance, a baseline window W_{base} is selected (see also our prior rolling window TRM study for detailed sensitivity results) [14].

To improve responsiveness under rapidly changing conditions, the window length is adjusted dynamically using the volatility change rate shown in Equation (32).

$$\mathrm{R}(t) = \frac{\sigma_t - \sigma_{t-\Delta t}}{\sigma_{t-\Delta t}} \tag{32}$$

And adaptive window length is then computed using Equation (33).

$$W(t) = W_{base} - \alpha|R(t)| \tag{33}$$

where $R(t)$ is the window adjustment increment determined by the volatility tracking rule, and Δt is the dispatch interval (5 min).

The adjustment coefficient α is given by Equation (34).

$$\alpha = \frac{W_{base} - W_{min}}{|R|_{max}} \tag{34}$$

Here, $|\ R\ |_{max}$ is set to the 95th percentile of observed $|\ R(t)\ |$ over the calibration dataset to reduce sensitivity to extreme outliers. The adaptive window is, finally, bounded as shown in Equation (35).

$$W_{min} \leq W(t) \leq W_{max} \tag{35}$$

with $W_{min} = 15$ min to preserve statistical validity, and $W_{max} = 60$ min to align with hourly operational planning.

This mechanism contracts the window during high-volatility intervals and expands it under stable conditions, improving the timeliness and reliability of dynamic TRM estimation.

3.10. Adaptive ATC Formulation with Adaptive TRM

Traditionally, TRM is computed using a fixed confidence factor K under the assumption that forecast errors are approximately Gaussian, so that a selected reliability level (e.g., 95%) maps directly to a constant quantile multiplier. While convenient, this static assumption becomes inadequate in renewable-dominated and non-stationary operating conditions where forecast error dispersion varies over time. To address this, the proposed framework generalizes the classical confidence factor formulation by introducing a time-varying confidence factor $K(t)$ that adapts to observed uncertainty dynamics, without requiring strict normality. The resulting dynamic TRM is given by Equation (36).

$$TRM_t = K(t) \times \sigma_{e,t} \tag{36}$$

where $\sigma_{e,t}$ represents the standard deviation of the forecast error at time t.

Operationally, TRM is updated at each time step t as follows: The rolling window retains the most recent W forecast error samples, and the rolling standard deviation $\sigma_{e,t}$ in Equation (27) quantifies the current volatility level. The adaptive confidence factor $K(t)$ in Equation (28) then expands or contracts the Gaussian multiplier according to how the current volatility compares with the reference level σ_{ref}. The time-varying margin is finally computed as $\mathrm{TRM}_t = K(t)\ \sigma_{e,t}$. This mechanism causes TRM to increase during volatile transitions, thereby strengthening system protection when uncertainty is elevated, and to decrease during calm low-uncertainty periods, thereby releasing transfer capability for renewable export. The resulting online update requires only $O(W)$ operations per step, making it suitable for real-time dispatch timescales.

The ATC at time t is computed following the NERC definition, with time variation arising from the operating condition-dependent TTC and the dynamic reliability margin given by Equation (37).

$$ATC_t = TTC_t - ETC - TRM_t \quad (37)$$

Here, TTC_t is obtained from AC power flow assessment under the adopted security constraints, ETC represents existing transmission commitments, and TRM_t is the dynamic transmission reliability margin updated from rolling uncertainty statistics. This yields an adaptive ATC trajectory that expands or contracts with prevailing uncertainty and constraint activity.

4. Case Studies, Data Description, and Simulation Setup

The proposed probabilistic ATC framework with dynamic TRM is validated on the IEEE 39-bus New England test system, a standard benchmark for transfer capability and reliability studies [19]. The system comprises 39 buses, 10 synchronous generators, 46 branches (34 lines and 12 transformers), and 19 load buses, with a base-case demand of 6097.1 MW and 1408.9 Mvar. Due to its interconnected structure and non-uniform transfer patterns, it is widely used for inter-area power flow and ATC assessment under uncertainty [28].

4.1. System Topology and Area Definition

The IEEE 39-bus New England system is partitioned into three interconnected areas for inter-area transfer capability assessment, consistent with standard practice in oscillatory stability and transfer capability studies (Figure 4). Area 1 (buses 1–3, 17–18, 25–30, 37–39) is the primary exporting region and includes generators G1 (bus 30), G8 (bus 37), G9 (bus 38), and G10 (bus 39). Area 2 (buses 4–8, 10–14, 31–33) represents the main importing region and includes generators G2 (bus 31), G3 (bus 32), and G4 (bus 33). Area 3 (buses 9, 15–16, 19–24, 34–36) serves as an intermediate transfer region and includes generators G5 (bus 34), G6 (bus 35), and G7 (bus 36).

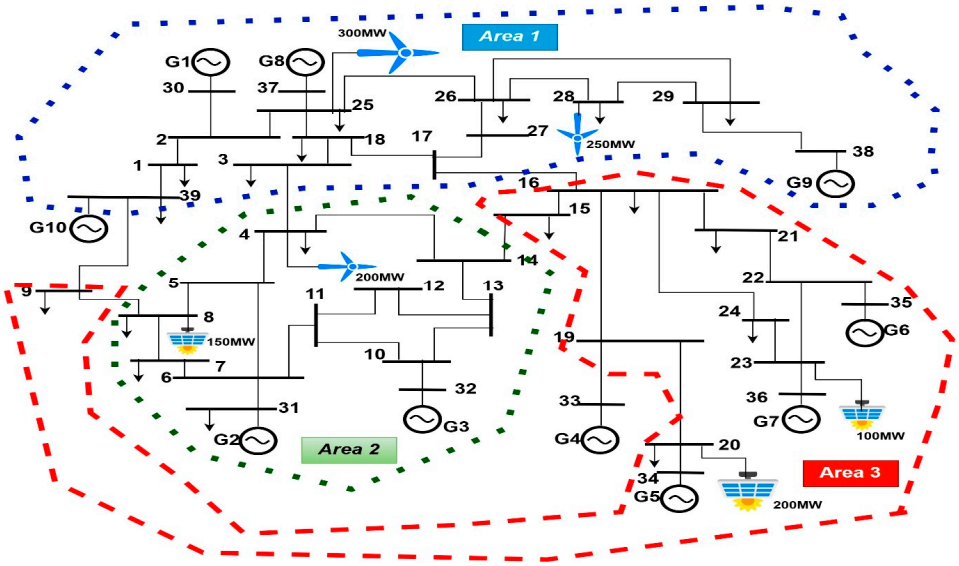

Figure 4. IEEE 39-bus New England test system.

The assessed transfer interface between Areas 1 and 2 comprises tie-lines 2–3, 3–4, 16–17, 17–18, 25–26, and 26–27, which are monitored for thermal limit violations during ATC evaluation. Generator G2 (bus 31) is selected as the slack bus, while all other generators operate in PV mode with voltage setpoints maintained within 0.98–1.05 p.u.

The Area 1 → Area 2 transfer interface represents a transmission corridor through which renewable generation from the exporting region must flow to reach load centers analogous to the transmission–distribution interface at grid supply points where distributed renewable export is governed by upstream transfer capability.

4.1.1. Renewable Generation Integration

Renewable generation profiles for the IEEE 39-bus system are synthesized from the specified probability distributions (Weibull for wind speed, Beta for solar irradiance) via Latin Hypercube Sampling, representing stochastic realizations consistent with the statistical parameters in Table 1 rather than historical measurement records. To represent renewable-rich operating conditions, wind and solar generation are integrated at selected buses in each area (Table 1). The total installed renewable capacity is 1200 MW (≈20% of peak load), representing a moderate-to-high penetration scenario.

Table 1. Renewable generation configuration and uncertainty models for the IEEE 39-bus system.

S/N	Bus	Generator	Type	Area	Capacity (MW)	Distribution Parameters
1	25	W1	Wind	1	300	Weibull (k = 2.0, c = 8.0 m/s)
2	28	W2	Wind	1	250	Weibull (k = 2.0, c = 8.0 m/s)
3	4	W3	Wind	2	200	Weibull (k = 2.2, c = 7.5 m/s)
4	8	PV1	Solar PV	2	150	Beta ($\alpha = 2.0,\ \beta = 5.0$)
5	20	PV2	Solar PV	3	200	Beta ($\alpha = 2.0,\ \beta = 5.0$)
6	23	PV3	Solar PV	3	100	Beta ($\alpha = 2.0,\ \beta = 5.0$)

Total installed renewable capacity: 1200 MW (appr. 20% of system peak load).

Wind capacity is concentrated in Area 1 (buses 25 and 28) to reinforce its exporting role, with additional wind generation in Area 2 to capture inter-area variability. Solar PV is placed in Areas 2 and 3 (buses 8, 20, and 23) to introduce variability in importing regions. Wind speed uncertainty is modeled using a Weibull distribution and mapped to power via the turbine power curve, while solar irradiance uncertainty is modeled using a Beta distribution on normalized irradiance. To reflect spatial diversity, modest parameter variations are applied across renewable units while maintaining consistent moderate-variability conditions across areas.

4.1.2. Load Uncertainty Parameters

Following the load uncertainty model in Section 3.4.1, short-term load forecast errors are parameterized using a 3% coefficient of variation ($\sigma = 0.03\ P_{\text{forecast}}$), consistent with typical day-ahead and intra-day forecasting accuracy reported in transmission operation studies. Load uncertainty is applied to the 19 demand buses according to the standard IEEE 39-bus load distribution, with the highest load concentrations at buses 3, 4, 7, 8, 15, 16, 18, 21, 23–29. This preserves the benchmark's spatial load characteristics while introducing realistic variability.

4.1.3. Transmission Line Thermal Uncertainty

Transmission constraint uncertainty is modeled as stochastic variation in the effective thermal limits of the critical corridor elements (Section 3.4.5). A truncated normal perturbation is applied to the six tie-lines forming the Area 1–Area 2 transfer interface, with $\sigma_\varepsilon = 3\%$ and bounds $\varepsilon_{\max} = \pm 8\%$, representing short-term variability due to ambient conditions (temperature and wind cooling) and modeling uncertainty commonly reported in operational studies [29]. All other lines retain their nominal thermal ratings and are treated

deterministically, consistent with the assumption that transfer capability is governed by a limited set of binding corridor constraints.

4.1.4. Simulation Parameters (IEEE 39-Bus System)

The key simulation parameters adopted for the IEEE 39-bus case study are summarized in Table 2.

Table 2. Simulation parameters for IEEE 39-bus case study.

Parameter	Value	Unit
Number of LHS scenarios (N)	1000	—
Baseline rolling window (W_base)	30	min
Minimum adaptive window (W_min)	15	min
Maximum adaptive window (W_max)	60	min
Baseline confidence factor (K_base)	1.645	—
Load forecast error CoV (σ_load)	3	%
Line thermal uncertainty std. dev. (σ_ε)	3	%
Line thermal uncertainty bounds (ε_max)	±8	%
Wind speed Weibull shape (k)	2.0	—
Wind speed Weibull scale (c)	8.0	m/s
Solar irradiance Beta parameters (α, β)	2.0, 5.0	—
Newton–Raphson convergence tolerance	10^{-6}	p.u.
Simulation time horizon	24	h
Time step resolution	5	min

4.2. New Zealand System Validation

4.2.1. Data Sources and Preprocessing

To demonstrate applicability beyond benchmark systems, the proposed probabilistic ATC framework with dynamic TRM is validated using operational data from New Zealand's power system. Half-hourly North Island (NI) grid-connected load demand and South Island (SI) wind generation are obtained from the Electricity Authority's Electricity Market Information (EMI) datasets for January–December 2024 [30]. NI demand is used as a system-level proxy for load-driven uncertainty, while SI wind represents weather-driven renewable variability relevant to NI–SI transfer requirements. The NI load series is filtered to retain grid-connected offtake consistent with system demand representation (Generation Type = GN). SI wind generation is formed by aggregating all EMI "Wind" units in the SI generation dataset to produce a system-level wind profile. Both time series are aligned to a common 30 min timestamp to ensure matched samples for correlation analysis and rolling window estimation, yielding synchronized inputs for evaluating dynamic TRM performance under real-world non-stationary conditions. The HVDC corridor constitutes a physical interface between renewable-rich South Island generation and North Island demand centers, providing a real-world analogue of the transmission–distribution boundary where upstream transfer capability governs renewable export.

A limitation of the New Zealand validation is the use of system-level aggregate proxies (total NI demand and total SI wind generation) rather than bus-level nodal data. This aggregation masks spatial heterogeneity in forecast errors and may therefore underestimate TRM when localized errors create network stress that is partially hidden by aggregation, or

overestimate TRM when localized effects offset one another. For the NZ HVDC corridor, however, this limitation is mitigated by the physical configuration: the HVDC link forms a single transfer bottleneck between the two islands, so inter-island transfer capability is governed primarily by aggregate NI–SI power balance rather than by detailed intra-island spatial distribution. The IEEE 39-bus benchmark, which employs bus-level uncertainty representation and full AC power flow, complements the NZ validation by demonstrating framework performance under spatially resolved uncertainty.

4.2.2. Statistical Characteristics

Table 3 summarizes the New Zealand datasets. The NI load series contains 17,566 half-hourly samples with mean 2629 MW (min 1488 MW; max 4297 MW) and standard deviation 540 MW. The SI wind series also contains 17,566 samples; with 58 MW installed capacity, it has mean output 18.5 MW (min 0 MW; max 52.5 MW) and standard deviation 17.2 MW, corresponding to an average capacity factor of 31.9%. The correlation between NI demand and SI wind is weak ($\rho = 0.029$), indicating near-independent load-driven and weather-driven variability and providing a realistic basis for evaluating rolling window dynamic TRM under non-stationary uncertainty.

Table 3. New Zealand system validation data characteristics.

Parameter	NI Load	SI Wind
Data source	EMI Grid Export	EMI Generation
Period	January–December 2024	January–December 2024
Resolution	30 min	30 min
Number of samples	17,566	17,566
Installed capacity (MW)	—	58
Mean (MW)	2629	18.5
Maximum (MW)	4297	52.5
Minimum (MW)	1488	0
Standard deviation (MW)	540	17.2
Capacity factor (%)	—	31.9
Correlation coefficient	0.029	—

NI = North Island; SI = South Island. Load data filtered for grid-connected offtake (Generation Type = GN). Wind generation from White Hill wind farm.

4.2.3. Validation Parameters

Inter-island transfer capability in New Zealand is governed by the HVDC Inter-Island link between the North and South Islands, making it the critical path for validation. The baseline rolling window size is $W_{\text{base}} = 48$ samples (24 h of half-hourly data), while the adaptive mechanism (Section 3.10) allows the window to vary between $W_{\min} = 12$ samples (6 h) and $W_{\max} = 336$ samples (7 days). The 24 h baseline captures the dominant diurnal cycling in NI demand, whereas the 7-day upper bound accommodates slower multi-day volatility patterns present in the year-long dataset. The confidence factor is fixed at $K = 1.645$, consistent with the baseline one-sided 95% quantile used in benchmarking.

The nominal HVDC capacity limits are 1050 MW northward and 750 MW southward, aligned with operational transfer constraints used for validation [31]. All validation parameters are summarized in Table 4.

Table 4. Framework parameters for New Zealand HVDC validation.

Parameter	Value	Unit
Number of LHS scenarios (N)	1000	—
Baseline rolling window (W_base)	48	Samples (24 h)
Minimum adaptive window (W_min)	12	Samples (6 h)
Maximum adaptive window (W_max)	336	Samples (7 days)
Baseline confidence factor (K_base)	1.645	—
K(t) bounds [K_min, K_max]	[1.10, 2.00]	—
Time resolution	30	Minutes
Critical transfer path	HVDC Inter-Island	—
HVDC TTC (northward)	1050	MW
HVDC capacity (southward)	750	MW

4.3. Evaluation Protocol and Benchmark Policies

This subsection defines the evaluation protocol used to compare TRM formulations under identical uncertainty realizations and establishes a benchmark set ranging from conventional deterministic practice to the fully adaptive TRM policy proposed in this work. Defining these benchmark policies prior to presenting the results ensures that performance differences in Section 5 are directly attributable to specific modeling choices (volatility tracking, confidence factor scheduling, or brute-force probabilistic margining).

4.3.1. Uncertainty Propagation Workflow (LHS + Iman-Conover + AC Power Flow)

For the IEEE 39-bus benchmark, uncertainty is propagated through the full AC network model using a scenario-based TTC evaluation pipeline. At each operating condition, uncertain inputs load demand, wind generation, solar generation, and selected corridor thermal limits are sampled via LHS and reordered using the Iman-Conover method to enforce the target rank correlation structure. Each scenario is solved using full AC power flow (Newton-Raphson, MATPOWER), and the Area 1 $\rightarrow$ Area 2 TTC is obtained by incrementally scaling the inter-area transfer until the first binding constraint occurs. A constraint is binding if (i) any monitored corridor element exceeds its thermal rating or (ii) any bus voltage violates 0.95–1.05 p.u. The resulting TTC samples form an empirical TTC distribution, from which volatility indicators and reliability margins are computed to benchmark the TRM policies.

4.3.2. Benchmark Set and Baseline Definition (Four Approaches)

Four TRM policies are evaluated on the same 24 h (5 min) operating trajectory to quantify the incremental benefits of (i) volatility tracking via $W(t)$ and (ii) adaptive confidence scheduling via $K(t)$:

1. Static %TRM (industry practice): TRM $= 0.075$ TTC.
2. Fixed-K rolling baseline: $W(t)$ adaptive, $K = K_{\text{base}} = 1.645$.
3. P95 pooled Monte Carlo margin: Constant TRM set to the 95th percentile of $|\ \Delta\text{TTC}\ |$ from sampled deviations.
4. Proposed adaptive TRM: Both $W(t)$ and $K(t)$ are adaptive (Equations (28)–(34)).

All approaches use identical TTC computation and uncertainty realizations; only the TRM policy differs. Approach 3 retains adaptive $W(t)$ while fixing K, isolating volatility

tracking, whereas Approach 4 adapts both $W(t)$ and $K(t)$, isolating the incremental value of confidence scheduling.

5. Simulation Results

5.1. LHS Convergence and Sampling Validation (TTC Snapshot)

LHS convergence is evaluated for the IEEE 39-bus Area 1 → Area 2 corridor under a stressed operating condition (peak demand ≈ 6097 MW). For $N = 100$–2000 scenarios, uncertainties (load, wind, solar, and selected corridor thermal limits) are sampled using LHS, correlated via Iman-Conover, and propagated through AC power flow (MATPOWER). TTC is obtained by scaling the inter-area transfer across tie-lines 2–3, 3–4, 16–17, 17–18, 25–26, and 26–27 until the first thermal or voltage violation (0.95–1.05 p.u.) occurs.

Figure 5 shows rapid stabilization of TTC statistics with increasing N. The mean TTC converges quickly to ≈ 1035 MW and varies by less than 0.08 MW (≈ 0.01%) over $N = 100$–2000. Tail estimates are more sensitive at small N: the 5th percentile deviates most at $N = 200$ (3.88% relative to the $N = 2000$ reference of 685.88 MW) but stabilizes within 1.5% beyond $N \approx 500$. The TTC standard deviation ranges from 224 to 232 MW across N, reflecting mixed voltage- and thermal-limited tail behavior.

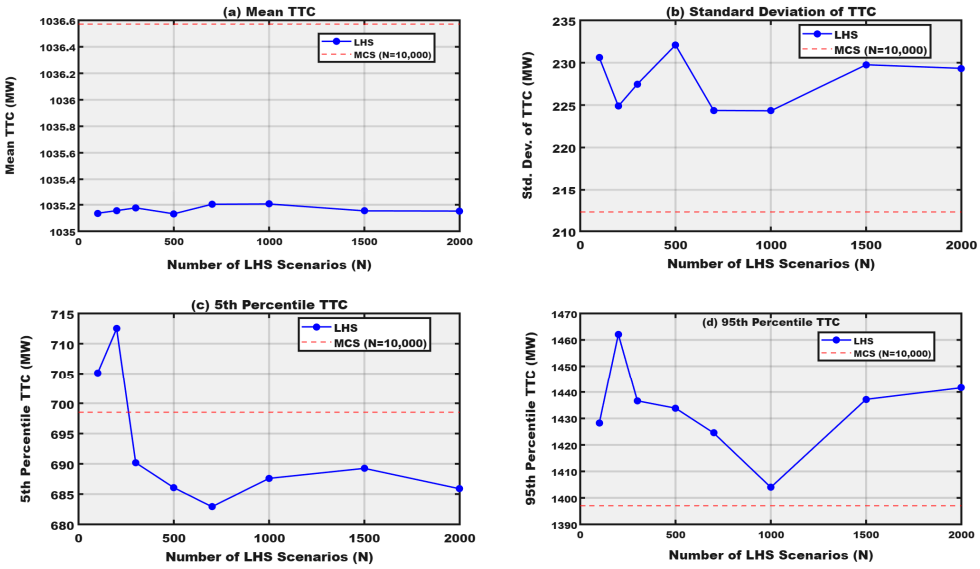

Figure 5. LHS convergence of TTC statistics for the IEEE 39-bus Area 1 → Area 2 transfer corridor under stressed loading (peak demand ≈ 6097 MW): (**a**) mean TTC, (**b**) standard deviation, (**c**) 5th percentile TTC, and (**d**) 95th percentile TTC versus number of LHS scenarios. Red dashed lines indicate the MCS reference values (N = 10,000).

To benchmark sampling efficiency, LHS-based TTC estimates at $N = 1000$ are compared with a conventional MCS using $N = 10,000$ independent samples drawn from the same marginals (without stratification or correlation control). As summarized in Table 5, LHS matches the MCS mean within 0.13% and the 5th/95th percentiles within 1.56%/0.50%, while reducing the computation time from 539.5 s to 62.7 s (8.6× speed-up). Accordingly, $N = 1000$ is adopted for subsequent analyses.

Table 5. Comparison of LHS (N = 1000) and MCS (N = 10,000) for TTC estimation.

Metric	LHS (N = 1000)	MCS (N = 10,000)	Relative Diff. (%)
Mean TTC (MW)	1035.21	1036.57	0.13
Std. Dev. of TTC (MW)	224.33	212.27	5.68

Table 5. *Cont.*

Metric	LHS (N = 1000)	MCS (N = 10,000)	Relative Diff. (%)
5th Percentile TTC (MW)	687.60	698.52	1.56
95th Percentile TTC (MW)	1403.98	1397.03	0.50
Computation Time (s)	62.70	539.50	--
Speed Ratio	--	--	8.6×

5.2. TTC Uncertainty Propagation and Source Contribution (IEEE 39-Bus)

Having established in Section 5.1 that $N = 1000$ LHS scenarios provide adequate convergence, this subsection characterizes the probabilistic TTC distribution obtained under joint uncertainty in load demand, wind generation, solar generation, and corridor thermal limits, propagated through full AC power flow with simultaneous thermal and voltage constraints. The resulting distribution (shape, dispersion, and tails) defines the uncertainty envelope that TRM must accommodate and forms the probabilistic basis for subsequent TRM and ATC evaluation.

Figure 6 shows the TTC probability density for the Area 1 → Area 2 corridor under the peak load operating condition. TTC is computed as the maximum inter-area transfer before the first binding constraint occurs—either a corridor thermal limit violation or a bus voltage deviation outside 0.95–1.05 p.u. The resulting distribution has mean 1035.22 MW and standard deviation 226.05 MW (CoV = 21.84%), spanning 516.94–1585.16 MW, with 5th and 95th percentiles of 681.79 MW and 1406.79 MW, respectively (90% interval width = 724.99 MW). The distribution is distinctly non-Gaussian and platykurtic (skewness = 0.106, kurtosis = 2.23), consistent with a mixed-regime TTC response under dual constraints: during low renewable output and weaker voltage support, voltage limits bind at lower transfer levels, whereas under favorable renewable injections, TTC shifts into a higher-transfer regime governed by thermal constraints. This regime switching implies that a fixed Gaussian-based multiplier (e.g., $K = 1.645$) may not uniformly represent tail risk across operating conditions, motivating the volatility-responsive confidence factor $K(t)$ introduced in Section 3.9. The observed non-Gaussian TTC distribution raises the question of whether a fully nonparametric quantile-based TRM, for example, using empirical lower-tail percentiles, would be more appropriate than the standard deviation-based formulation in Equation (36). Three observations are relevant. Firstly, the adopted formulation with dynamic $K(t)$ provides an empirically calibrated quasi-quantile margin, since $K(t)$ adapts the multiplier in response to observed volatility rather than assuming strict Gaussianity. Secondly, the TTC distribution in this case is platykurtic $(\text{kurtosis} = 2.23 < 3.0)$, indicating lighter tails than a Gaussian distribution and suggesting that a fixed Gaussian-based multiplier such as $K = 1.645$ may be mildly conservative under the studied operating condition. Thirdly, a fully nonparametric quantile-based TRM would require repeated estimation of tail percentiles from short rolling samples; for $W = 15$ min at 5 min resolution, this yields only three samples, which are too few for stable percentile estimation. Nevertheless, for systems exhibiting strongly skewed or heavy-tailed TTC behavior, quantile regression or distribution-free TRM formulations may offer a useful extension and are therefore identified as future work.

5.2.1. Uncertainty Source Decomposition

To identify dominant drivers of TTC uncertainty, four LHS runs are conducted by activating one uncertainty source at a time while holding others at nominal values: A (load only), B (renewables only: wind + solar), C (corridor thermal ratings only), and D (all sources combined). Each case uses 1000 scenarios propagated through AC power flow and

the dual-constraint TTC procedure. Source contributions are obtained by normalizing each isolated-case TTC variance by the combined-case variance.

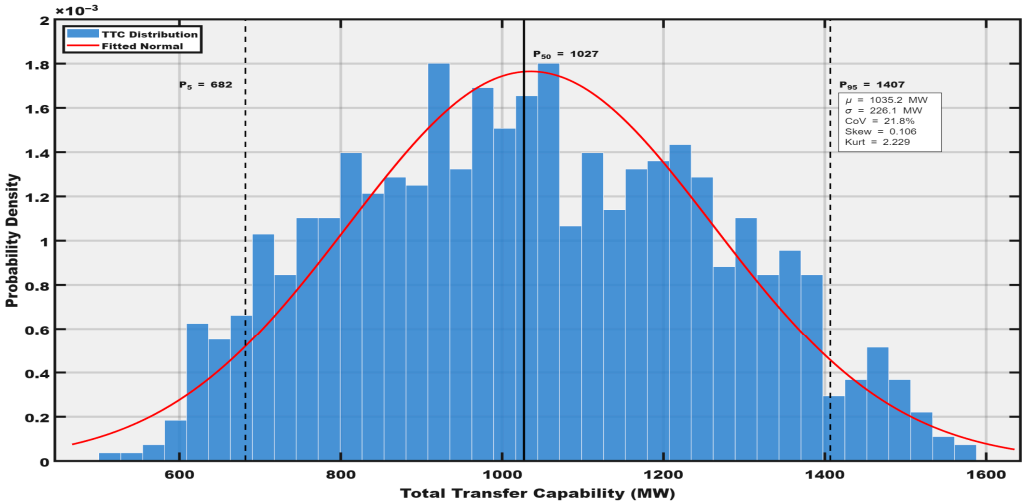

Figure 6. Empirical TTC distribution for the IEEE 39-bus Area 1 → Area 2 corridor under peak load conditions (N = 1000 LHS scenarios). The histogram shows the scenario-based TTC density; the red curve is a fitted normal distribution. Vertical lines indicate P_5, P_{50}, and P_{95}, highlighting the non-Gaussian, mixed-regime TTC behavior under simultaneous thermal and voltage constraints.

Table 6 shows that renewable uncertainty dominates TTC variance, contributing 96.7% of total TTC variance ($\sigma = 222.31$ MW), while load uncertainty contributes 5.6% ($\sigma = 53.29$ MW). Thermal rating uncertainty contributes 0%, indicating that under simultaneous voltage and thermal enforcement, ±3% tie-line rating perturbations do not materially affect the binding constraint: in voltage-limited intervals, TTC is governed by bus voltage limits, and in thermal-limited intervals, the ±3% rating shift is only a few MW relative to the hundreds of MW variability induced by renewable fluctuations. The isolated contributions sum to 102.3%, yielding a small negative interaction of −2.3%, consistent with partial cancellation under joint uncertainty through network power redistribution. Overall, these results justify a renewable-driven time-varying TRM while retaining joint load–renewable modeling. Figure 7 summarizes the source decomposition, showing standard deviations (a) and variance share contributions (b) for each isolated and combined uncertainty case.

Table 6. Uncertainty source decomposition of TTC variance.

Uncertainty Source	Mean TTC (MW)	Std Dev (MW)	Variance (MW^2)	% of Total Variance
A: Load only	1046.90	53.29	2840.0	5.6
B: Renewables only	1035.27	222.31	49,422.6	96.7
C: Line thermal only	1046.99	0.00	0.0	0.0
Nonlinear interaction	—	—	—	−2.3
D: All combined	1035.22	226.05	51,099.5	100.0

The near-zero contribution of thermal rating uncertainty reflects the specific operating regime studied. When voltage limits bind, as in many scenarios of the IEEE 39-bus corridor, TTC is governed by bus voltage stability rather than by small changes in line thermal ratings, so ±3% thermal limit perturbations do not materially shift the binding constraint. Even in thermal-limited intervals, the corresponding rating variation is only a few megawatts, which is small relative to the much larger TTC variability induced by renewable fluctuations.

Under higher thermal rating variability or in purely thermal-limited corridors, constraint-side uncertainty would contribute more substantially. The framework retains this modeling capability and therefore generalizes to such regimes without structural modification.

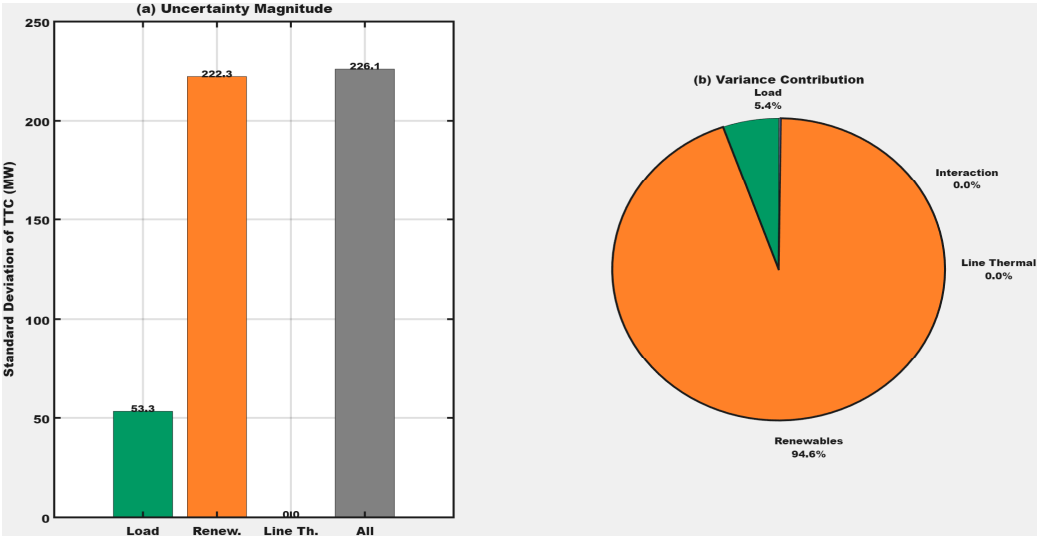

Figure 7. TTC uncertainty source decomposition for the IEEE 39-bus Area 1 → Area 2 corridor (N = 1000 LHS): (**a**) standard deviation of TTC under isolated and combined uncertainty cases; (**b**) variance share contribution of load, renewables, and line thermal uncertainty (including interaction term).

5.2.2. Effect of Correlation Control

Iman–Conover rank correlation control (Section 3.3) is used to enforce the target dependence structure among uncertain inputs in the LHS scenarios. To quantify its impact, the $N = 1000$ analysis is repeated with correlation control disabled (independent LHS without rank reordering). Table 7 summarizes the statistics.

Table 7. Effect of Iman–Conover correlation control on TTC statistics.

Metric	With Correlation	Without Correlation	Difference
Mean TTC (MW)	1035.22	1035.36	−0.14
Std Dev (MW)	226.05	212.57	+13.48
5th Percentile (MW)	681.79	705.15	−23.35
95th Percentile (MW)	1406.79	1402.15	+4.64
90% CI Width (MW)	724.99	697.00	+27.99
Skewness	0.106	0.189	−0.083

Correlation control has negligible influence on the mean TTC (difference = 0.14 MW, ≈0.01%) but materially alters tail risk. With correlation control enabled, the 5th percentile decreases by 23.35 MW (681.79 MW vs. 705.15 MW), indicating higher downside risk than independent sampling suggests. The 90% interval widens by 27.99 MW (697.00 MW to 724.99 MW), and the standard deviation increases by 13.48 MW. These effects are amplified under dual thermal–voltage constraints because correlated stress patterns (e.g., higher load coincident with renewable shortfalls) increase the frequency of voltage-limited binding, producing lower TTC outcomes.

Consequently, ignoring dependence would underestimate lower-tail TTC and bias TRM downward by approximately the same magnitude, risking under-protected transfer allocations during stressed conditions.

To quantify correlation preservation quality, the element-wise root-mean-square error (RMSE) between the target rank correlation matrix and the realized sample rank correlation matrix was computed after Iman–Conover reordering for the $N = 1000$ scenario set. The resulting RMSE is 0.032, with a maximum absolute element-wise error of 0.100, indicating close agreement with the prescribed dependence structure. This fidelity is consistent with theoretical expectations for the Iman–Conover method at moderate sample sizes [25].

5.3. Rolling Window Forecast Error Analysis and Adaptive Volatility Estimation

Sections 5.1 and 5.2 characterize TTC uncertainty under a static snapshot. This subsection reports the resulting time-varying uncertainty profile $\sigma_{\mathrm{TTC}}(t)$ over a 24 h, 5 min trajectory, obtained using rolling statistics with an adaptive window. The $\sigma_{\mathrm{TTC}}(t)$ profile provides the volatility input used for the dynamic TRM computation in Section 5.4.

5.3.1. Forecast Error Time Series

A 24 h forecast error trajectory (288 samples) is synthesized for load, wind, and solar to emulate non-stationary diurnal behavior consistent with the NZ validation dataset. Errors exhibit persistence (AR (1)-type dependence) and time-varying dispersion, with the highest volatility occurring during ramp/transition periods (morning/evening load ramps and wind regime shifts). Full parameter settings (CoVs, time-of-day scaling, and autocorrelation coefficients) are provided in Section 4. Figure 8 shows the resulting forecast error trajectories with time-varying $\pm 1\sigma$ envelopes, illustrating the non-stationary diurnal volatility profile used for rolling $\sigma(t)$ estimation.

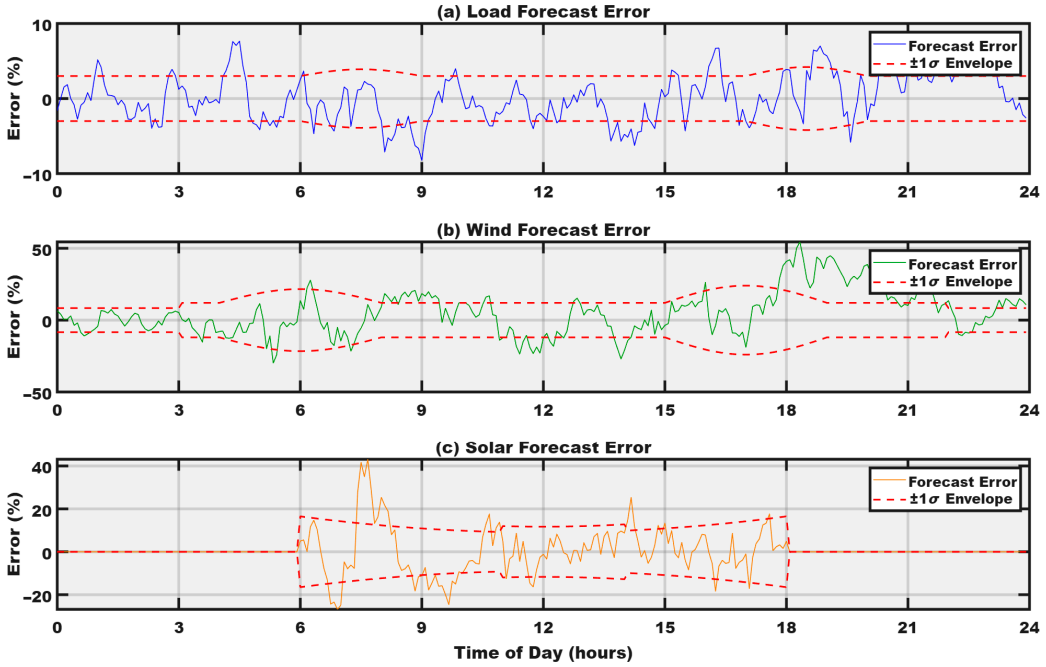

Figure 8. Synthetic 24 h (5 min) forecast error trajectories with time-varying ±1σ envelopes for (**a**) load forecast error, (**b**) wind forecast error, and (**c**) solar forecast error, illustrating the non-stationary diurnal volatility patterns used for rolling $\sigma(t)$ estimation.

5.3.2. Window Size Sensitivity Analysis

Before applying the adaptive window mechanism, a baseline window length W_{base} is selected. Candidate windows $W \in \{15, 30, 45, 60\}$ min are evaluated to span typical operational timescales (AGC to hourly scheduling). For each W, the rolling standard deviation σ_t (Equation (27)) and rolling RMSE (Equation (30)) are computed on the dominant wind forecast error series. Performance is assessed using two metrics: tracking error (volatility-

following accuracy) and estimation noise (variability in the σ_t estimate), capturing the responsiveness–stability trade-off.

Table 8 and Figure 9 show that $W = 15$ min tracks volatility changes fastest (four-step lag) but yields the noisiest estimates (31.63% noise). $W = 60$ min is least noisy (50.19% tracking error) but exhibits the largest delay (nine-step lag), which is undesirable for dynamic TRM. The $W = 30$ min window provides the best practical compromise, achieving moderate noise (29.06%) with acceptable tracking performance (61.91%) and an RMSE of 0.1327. Accordingly, $W_{\text{base}} = 30$ min is adopted for the adaptive mechanism, consistent with real-time dispatch timescales.

Table 8. Fixed-window sensitivity analysis for rolling volatility estimation: tracking error, estimation noise, mean RMSE, and response lag for candidate window lengths.

W (min)	Tracking Performance (%)	Estimation Noise (%)	Mean RMSE (Equation (30))	Lag (Steps)
15	73.62	31.63	0.1293	4
30	61.91	29.06	0.1327	6
45	54.72	27.91	0.1344	8
60	50.19	28.38	0.1354	9

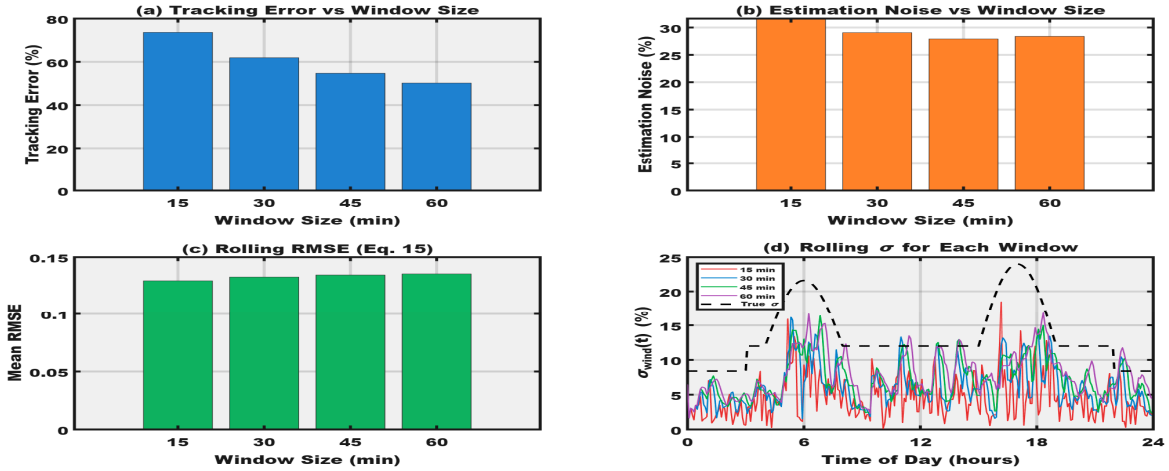

Figure 9. Fixed-window sensitivity analysis for rolling volatility estimation: (**a**) tracking error, (**b**) estimation noise, (**c**) mean RMSE, and (**d**) rolling $\sigma_{\text{wind}}(t)$ profiles for $W = \{15, 30, 45, 60\}$ min, illustrating the responsiveness–stability trade-off and supporting the choice of W_{base}.

5.3.3. Rolling Window Volatility Estimation with Adaptive Sizing

The instantaneous TTC uncertainty, $\sigma_{\text{TTC}}(t)$, is estimated using the rolling window standard deviation operator (Equation (27)) applied to the forecast error series over a trailing window of length $W(t)$. To retain diurnal tracking while improving responsiveness to sharp volatility transitions, an adaptive window-sizing mechanism (Section 3.9) is applied. The volatility change rate $R(t)$ is computed from consecutive rolling σ estimates (Equation (31)).

The adaptive window length $W(t)$ is then updated using the sizing law in Equation (32) and bounded using Equation (34) with $[W_{\min}, W_{\max}] = [15, 60]$ min. Calibration via Equation (33) at 5 min resolution yields $\alpha = 6.85$ and $|R|_{\max} = 0.4380$ (the P_{95} of $|R(t)|$). Rolling dispersions of load, wind, and solar forecast errors are mapped to MW-scale TTC uncertainty using the variance decomposition sensitivities from Section 5.2, preserving relative source contributions (e.g., $g_{\text{load}} = 53.29$ MW and $g_{\text{wind}} = 222.31$ MW per unit source-σ). Table 9 summarizes the resulting $\sigma_{\text{TTC}}(t)$ statistics for the adaptive, fixed-window, and static snapshot estimators.

Table 9. Comparison of $\sigma_{TTC}(t)$ estimation approaches.

Metric	Adaptive Window	Fixed Window (30 min)	Static (Snapshot)
Mean (MW)	115.07	121.57	226.05
Min (MW)	14.28	40.76	226.05
Max (MW)	343.92	299.84	226.05
Max/Min ratio	24.09	7.36	1.00
(% time)	93.8%	93.4%	—
Mean reduction vs. static	49.1%	46.2%	—

Adaptive window dynamics: Figure 10 shows that $|\ R(t)\ |$ spikes primarily during the morning (04:00–08:00) and evening (15:00–19:00) transitions; the P_{95} threshold $|\ R\ |_{\max}$ ensures window contraction is triggered only by significant volatility shifts. Consequently, $W(t)$ contracts toward $W_{\min} = 15$ min during volatile intervals and relaxes toward $W_{\text{base}} = 30$ min during stable periods. The mean window is 24.7 min, with $W_{\min}$ active for 9.7% of time steps and W_{base} for 35.8% (upper bound not reached). Table 9 confirms a strongly time-varying uncertainty profile with $\sigma_{\text{TTC}}(t)$ spanning 14.28–343.92 MW (max/min = 24.09). The adaptive estimate remains below the static snapshot for 93.8% of the horizon but exceeds it during the remaining 6.2% transition regimes, implying that a static margin would be over-conservative most of the time yet potentially under-protective during volatility peaks. Relative to the fixed 30 min window, adaptive sizing sharpens peaks (343.92 vs. 299.84 MW) and deepens troughs (14.28 vs. 40.76 MW), directly supporting the dynamic TRM scheduling in Section 5.4.

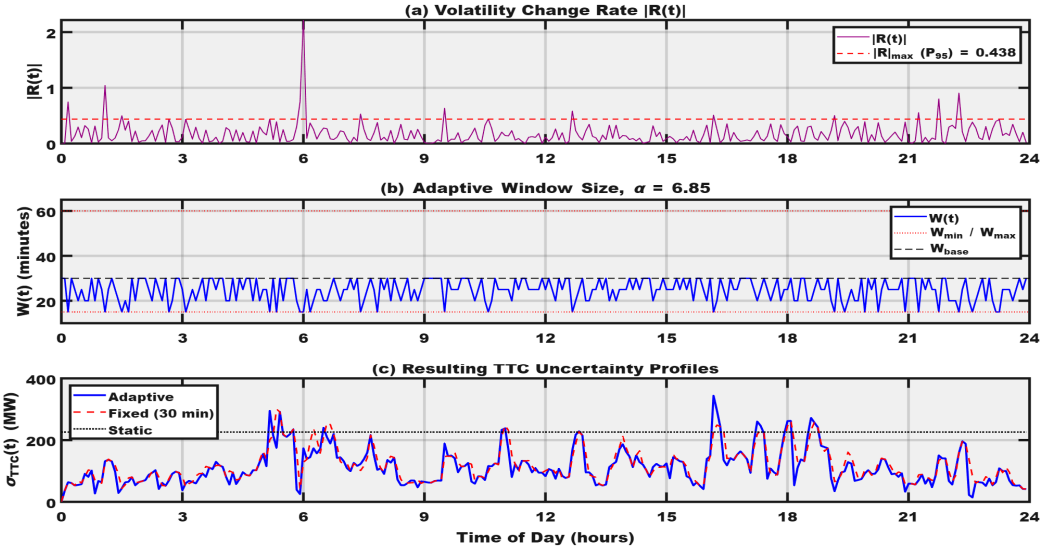

Figure 10. Adaptive window dynamics and resulting TTC uncertainty profile over a 24 h horizon. (**a**) Absolute volatility change rate $|\ R(t)\ |$ with the P_{95} threshold $|\ R\ |_{\max}$. (**b**) Adaptive window length $W(t)$ bounded by $W_{\min}$, W_{base}, and $W_{\max}$. (**c**) Resulting $\sigma_{\text{TTC}}(t)$ profiles comparing adaptive sizing, fixed 30 min window, and the static snapshot.

5.4. Dynamic Confidence Factor Scheduling and TRM Estimation

Section 5.3 showed that forecast error volatility is strongly non-stationary, with $\sigma_{\text{TTC}}(t)$ varying from 14.28 to 343.92 MW over the 24 h horizon under the adaptive rolling window estimator. The fixed-quantile rolling baseline (Approach 3; Section 4.3.2) converts this time-varying dispersion into a time-varying margin using a constant Gaussian multiplier, $\text{TRM}(t) = K_{\text{base}} \times \sigma_{\text{TTC}}(t)$ with $K_{\text{base}} = 1.645$. This section evaluates whether

additionally scheduling the confidence factor $K(t)$ via (28) (Approach 4) can recover additional ATC headroom without compromising reliability. All four benchmark TRM policies (Section 4.3.2) are assessed on the same 24 h, 5 min operating trajectory for the IEEE 39-bus transfer corridor, with TTC = 300MW.

5.4.1. Adaptive Confidence Factor $K(t)$

The scheduled confidence factor is computed from Equation (28) using $K_{\text{base}} = 1.645$, the renewable sensitivity coefficient $\beta = 0.5355$, and the reference uncertainty $\sigma_{\text{ref}} = \mathbb{E}[\sigma_{\text{TTC}}(t)] = 112.68$ MW. Here, β is obtained from Equation (29) as the ratio of combined renewable forecast error dispersion to net load dispersion, $\beta = \frac{\sqrt{\sigma^2_{\text{wind}} + \sigma^2_{\text{solar}}}}{\sigma_{\text{netload}}}$.

To avoid unrealistically small margins in calm periods and excessive conservatism during sharp volatility transitions, $K(t)$ is bounded to $[K_{\min}, K_{\max}] = [1.10, 2.50]$. These bounds are wider than the IEEE 30-bus benchmark $[1.28, 2.00]$ to accommodate the stronger renewable-driven variability in the present corridor ($\beta = 0.5355$ vs. 0.4618). Bound saturation occurs in 11.1% of time steps, indicating that the limiter serves mainly as a protective safeguard under extreme regimes rather than dominating the scheduling.

As shown in Figure 11, the scheduled multiplier preserves baseline reliability on average, with $\bar{K(t)} = 1.632$ (within 0.8% of K_{base}), while increasing during transition periods and decreasing in stable intervals. $K(t)$ reaches $K_{\max} = 2.50$ near the peak volatility period ($t \approx 5.17$ h) and attains $K_{\min} = 1.10$ during low-volatility periods. Table 10 summarizes the resulting $K(t)$ statistics.

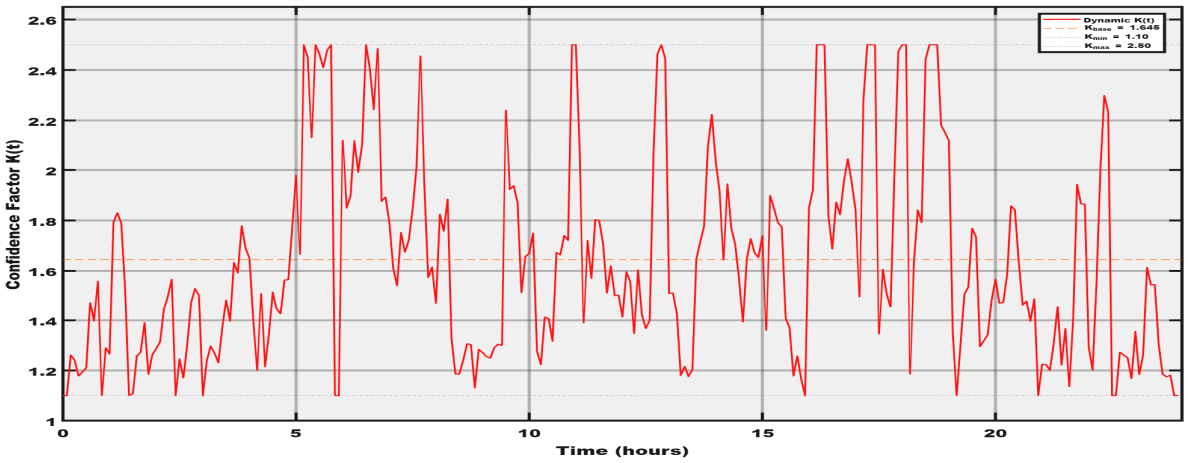

Figure 11. Scheduled confidence factor $K(t)$ under time-varying uncertainty (24 h horizon).

Table 10. Confidence factor statistics over the 24 h horizon (IEEE 39-bus).

Statistic	Approach 4: K(t)	Approach 3: K	Interpretation
Mean	1.632	1.645	Avg. reliability preserved ($\leq$0.8%)
Std. Dev.	0.402	0.000	Active scheduling range
Minimum	1.100 (=$K_{\min}$)	1.645	Relaxed in calm periods
Maximum	2.500 (=$K_{\max}$)	1.645	Tightened under stress
Range	1.400	0.000	Adaptation bandwidth
Saturation	11.1%	N/A	5.2% at $K_{\min}$, 5.9% at $K_{\max}$

5.4.2. Four-Way TRM and ATC Comparison

The resulting TRM(t) exhibits a clear diurnal pattern—expanding during the morning/evening transition regimes (Section 5.3) and contracting in stable intervals. Figure 12

shows the mean TRM/ATC allocation across all four approaches, while Figures 13 and 14 present the TRM and ATC time series profiles, respectively. Scheduling lowers the mean TRM from 186.01 MW to 170.81 MW and increases the mean ATC from 113.99 MW to 129.19 MW, while still allocating larger margins during the limited high-volatility intervals where a constant multiplier would be under-protective.

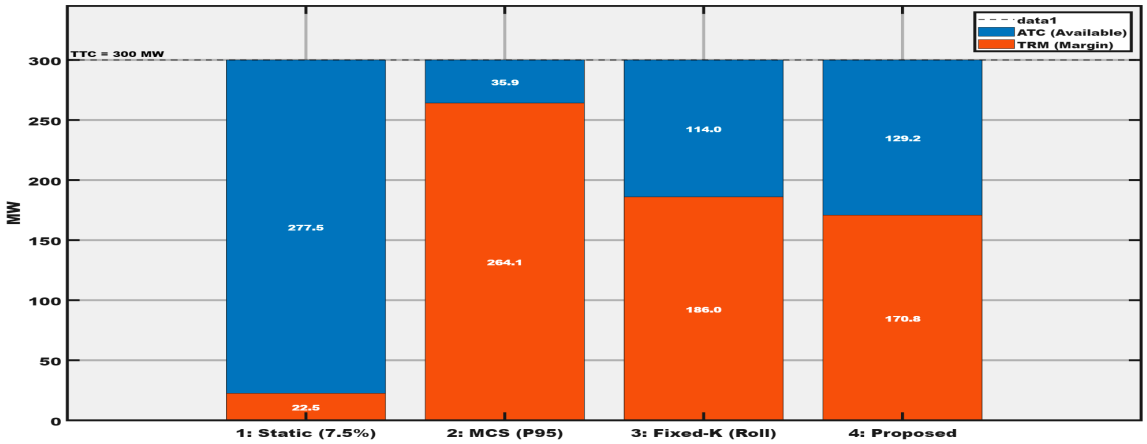

Figure 12. Mean TRM and ATC allocation across the four benchmark approaches (IEEE 39-bus, TTC = 300 MW).

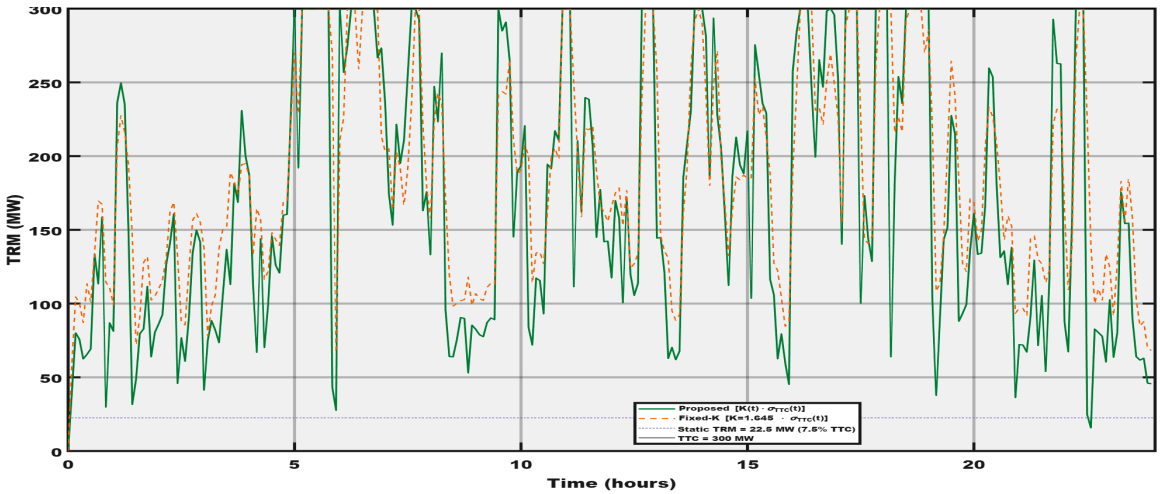

Figure 13. TRM time series from rolling σ(t): fixed-K baseline versus dynamic K(t).

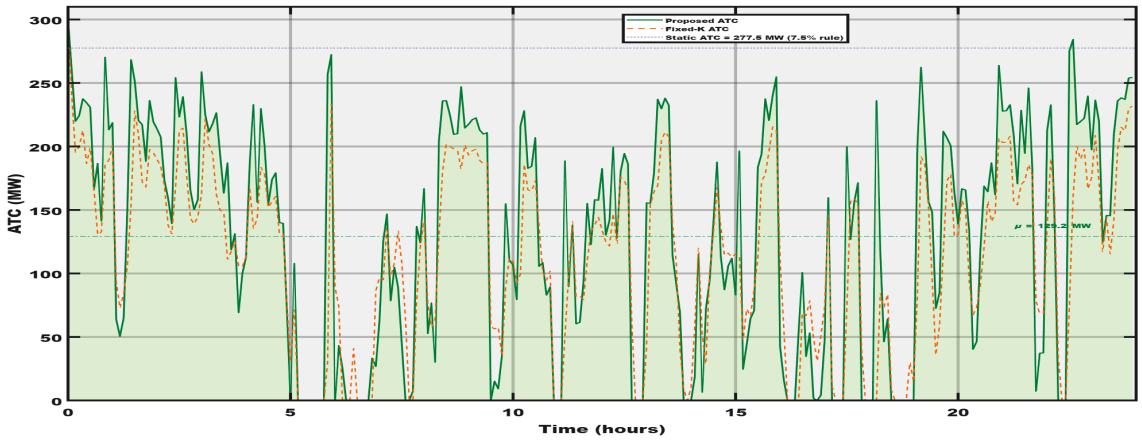

Figure 14. ATC profiles with rolling window TRM: dynamic $K(t)$ vs. fixed K_{base}.

Table 11 summarizes the four benchmark policies. As expected, the 7.5% rule is not risk-calibrated (typically under-margining), the pooled MCS P95 margin is anchored to worst-case intervals (over-margining), and rolling policies provide the most operationally relevant trade-off. Overall, the proposed method recovers substantial headroom relative to pooled MCS—raising the mean ATC from 35.88 MW to 129.19 MW (+260%) and reducing the mean TRM from 264.12 MW to 170.81 MW (−35%), i.e., reclaiming roughly 50% of TTC capacity compared to the pooled constant-margin policy.

Table 11. TRM and ATC comparison across four benchmark approaches (IEEE 39-bus, TTC = 300 MW).

Metric	1: Static (7.5%)	2: MCS (P95)	3: Fixed-K Rolling	4: Proposed Adaptive
Mean TRM (MW)	22.50	264.12	186.01	170.81
Mean ATC (MW)	277.50	35.88	113.99	129.19
TRM as % of TTC	7.5%	88.0%	62.0%	56.9%
Time constrained (%)	0.0%	0.0%	14.2%	18.1%
Adaptation ratio	1.0:1	1.0:1	5.0:1	19.1:1

Pairwise Comparison and Attribution of Improvements

Approach 1 (static) allocates only 22.50 MW—insufficient by more than an order of magnitude during volatile transitions where $\sigma_{\mathrm{TTC}}(t)$ exceeds 300 MW. Approach 2 (MCS) allocates 264.12 MW (88.0% of TTC), leaving only 35.88 MW usable ATC—probabilistically rigorous but operationally impractical because the pooled P95 is anchored to the 6.2% of high-volatility time steps that dominate the tail.

Table 12 decomposes the cumulative ATC recovery into its two framework components. Of the total 93.31 MW gain (Approach 2 → 4), temporal volatility tracking via rolling $\sigma_{\mathrm{TTC}}(t)$ contributes 78.11 MW (84%), while adaptive K(t) scheduling adds the remaining 15.20 MW (16%). Importantly, the constrained time fractions remain comparable across the two rolling approaches (14.2% for Approach 3 vs. 18.1% for Approach 4, Table 11), confirming that the capacity recovery arises from reduced over-margining during calm periods rather than weakened protection during stressed intervals. From a renewable integration perspective, this 93.31 MW of recovered ATC represents additional export headroom that would otherwise be unavailable to renewable generation at the transfer interface. In practical terms, unnecessary curtailment is reduced during the 81.9% intervals (100% − 18.1%, Table 11) when the corridor is unconstrained.

Table 12. Pairwise ATC improvements across benchmark approaches.

Comparison	ATC Gain (MW)	Relative Gain (%)	Source of Improvement
2 → 3 (MCS → Fixed-K)	+78.11	+217.7	Temporal resolution via rolling $\sigma_{\mathrm{TTC}}(t)$
3 → 4 (Fixed-K → Proposed)	+15.20	+13.3	K(t) scheduling (adaptation ratio 19.1:1 vs. 5.0:1)
2 → 4 (MCS → Proposed)	+93.31	+260.1	Cumulative: rolling window + confidence scheduling

The physical basis for the observed ATC recovery is straightforward. A pooled static margin must be calibrated to cover the highest volatility encountered over the full evaluation horizon, even though this condition occurs in only about 6% of time steps (Section 5.3).

During the remaining ∼ 94% of the horizon, the actual forecast error dispersion is substantially lower than the pooled estimate. By replacing this time-invariant margin with a rolling estimate that tracks instantaneous volatility, the proposed framework assigns smaller TRM during calm intervals, thereby releasing transfer capacity, and larger TRM during the relatively infrequent volatile intervals, thereby preserving protection. The dynamic $K(t)$ scheduling further sharpens this temporal reallocation by decreasing the confidence multiplier when $\sigma_t < \sigma_{\text{ref}}$ and increasing it when $\sigma_t > \sigma_{\text{ref}}$, thereby recovering additional headroom in proportion to the normalized deviation from the reference uncertainty level.

5.4.3. Margin Utilization and Operational Tightness

To quantify operational tightness, TRM is normalized by TTC. The proposed method (Approach 4) yields the lowest average margin utilization among the probabilistic policies (56.9%), compared with 62.0% (Approach 3), 88.0% (Approach 2), and 7.5% (Approach 1). The reduction from 88.0% $\rightarrow$ 62.0% $\rightarrow$ 56.9% confirms that (i) rolling $\sigma_{\text{TTC}}(t)$ recovers headroom by avoiding worst-case pooling, and (ii) $K(t)$ scheduling provides additional de-conservatism in low-volatility regimes. The proposed method is constrained (ATC ≈ 0) for 18.1% of the horizon versus 14.2% for Approach 3, indicating ATC gains primarily arise from reduced over-margining during stable periods, not relaxed protection during stressed intervals.

Figure 15a compares the TRM distributions for Approaches 3–4, with the constant MCS TRM (264.12 MW) and static TRM (22.50 MW) shown as references. The MCS value lies near the upper tail of the rolling distributions, confirming it is dominated by infrequent high-volatility events. Figure 15b shows the ATC duration curves: the proposed method exceeds the fixed-K baseline for ~85% of the period and both rolling methods dominate the MCS policy, while the static rule yields the highest nominal ATC but without probabilistic protection.

5.4.4. Sensitivity Analysis of β on TRM and ATC Performance

The scaling coefficient β in (30) governs how strongly the confidence factor $K(t)$ responds to deviations in the volatility measure $\sigma_{\text{adaptive}}(t)$. A larger β increases the responsiveness of $K(t)$, producing stronger margin expansion during high-uncertainty periods and stronger contraction during low-uncertainty periods. To assess the robustness of the proposed method, β was perturbed by $\pm 30\%$ around its data-derived value ($\beta = 0.5355$), and the full 24 h TRM/ATC trajectory was recomputed for each case.

Table 13 summarizes the resulting mean TRM and ATC values. The results show a smooth and monotonic response. Reducing β by 30% yields a slightly higher mean TRM of 172.39 MW and a correspondingly lower mean ATC of 127.61 MW, whereas increasing β by 30% yields a slightly lower mean TRM of 169.47 MW and a higher mean ATC of 130.53 MW. The baseline case ($\beta = 1.0\times$) lies naturally between these two extremes, with a mean TRM of 170.81 MW and mean ATC of 129.19 MW.

Table 13. Sensitivity of mean TRM and mean ATC to β scaling in the proposed adaptive framework.

β Setting	Mean TRM (MW)	Mean ATC (MW)
0.7 × β	172.39	127.61
1.0 × β	170.81	129.19
1.3 × β	169.47	130.53

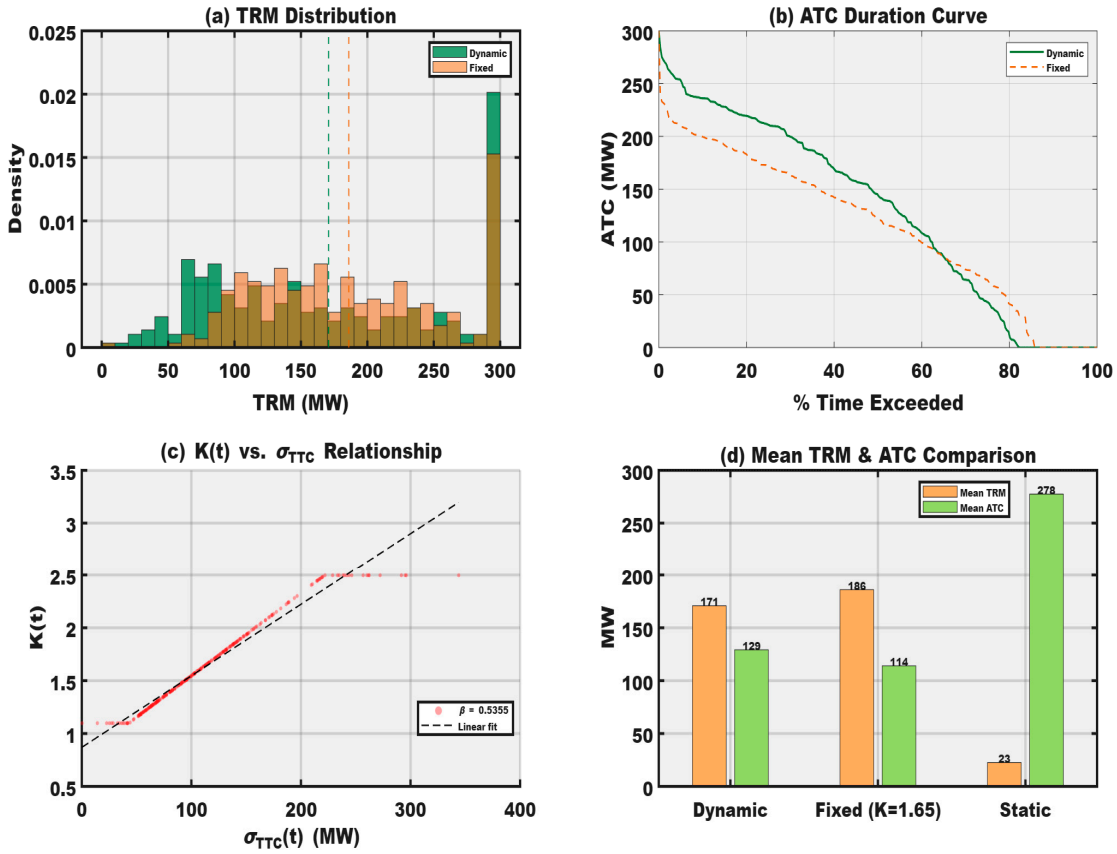

Figure 15. Margin utilization and confidence factor analysis for the IEEE 39-bus system (TTC = 300 MW). (**a**) TRM probability distributions for Approaches 3 (fixed-K) and 4 (proposed) (orange-brown), with MCS-based TRM (264.12 MW, red dashed) and static TRM (22.50 MW, green dashed) as reference lines. (**b**) ATC duration curves comparing proposed and fixed-K policies. (**c**) Relationship between scheduled confidence factor K(t) and rolling volatility $\sigma_{\mathrm{TTC}}(t)$, with fitted scaling coefficient β = 0.5355. (**d**) Mean TRM and ATC allocation for the three probabilistic benchmark approaches.

This behavior confirms that β acts primarily as a responsiveness gain rather than as a structural determinant of framework performance. Even under a $\pm$30% perturbation, the mean TRM changes by only about $\pm$1.5 MW, while the mean ATC changes by about $\pm$1.6 MW. These variations are small relative to the TTC scale and do not alter the principal operating conclusions. In particular, the adaptive framework remains well-conditioned and only mildly sensitive to the precise calibration of β. Across the $\pm$30% sensitivity sweep, the mean ATC remains within a narrow range of 127.61–130.53 MW (total spread: 2.92 MW), indicating that the proposed adaptive framework is robust to moderate perturbations in the responsiveness parameter.

Overall, the sensitivity sweep indicates that the value of β obtained from (30) is both reasonable and robust. Moderate deviations in β do not materially affect the method's behavior or its operational interpretation, confirming that the proposed volatility-aware TRM framework maintains consistent performance over a practical range of responsiveness settings.

5.5. Cross-System Validation with NZ Operational Data

The two validation cases operate at different but complementary abstraction levels. The IEEE 39-bus case provides a full bus-level probabilistic AC power flow analysis with simultaneous thermal and voltage constraints, whereas the New Zealand HVDC case applies corridor-level rolling window analysis using aggregate operational data. This

asymmetry is intentional: the IEEE benchmark demonstrates the framework's full capabilities under spatially resolved uncertainty and complete network modeling, while the NZ case demonstrates practical deployability using the type of real-world operational data readily available to TSOs. Together, the two studies show that the dynamic TRM mechanism performs consistently across both a synthetic network with full AC modeling and a real-world corridor with actual non-stationary uncertainty.

The four-way TRM comparison is repeated using half-hourly operational data from New Zealand's HVDC inter-island corridor (Benmore–Haywards), comprising North Island load and South Island wind generation from January–December 2024 (17,566 samples). Forecast errors are computed using one-step-ahead persistence (Equation (23), h = 30 min), and the corridor TTC is fixed at 1050 MW. The empirically derived parameters are $\beta_{NZ} = 0.6018$ and $\sigma_{ref} = 126.29$ MW. The resulting $\sigma_{TTC}(t)$ spans 12.77–323.89 MW (max/min = 25.36), confirming strongly non-stationary uncertainty comparable to the IEEE benchmark.

Temporal adaptation remains the dominant recovery mechanism: the rolling window transition (Approach 2 $\rightarrow$ 3) increases the mean ATC by 59.51 MW (+7.6%) on real operational data. In contrast, $K(t)$ scheduling yields only a 6.74 MW marginal TRM increase (-0.8% ATC change), compared with a 15.20 MW (+13.3%) gain on the IEEE corridor. This difference is explained by the congestion regime. On the IEEE corridor (TRM/TTC = 56.9%, 18.1% binding), the ATC floor truncates extreme $K(t)\ \sigma(t)$ realizations, allowing adaptive scheduling to reduce the mean TRM. On the NZ corridor (TRM/TTC = 20.4%, 0% binding), no truncation occurs, so scheduling provides negligible benefit. Table 14 summarizes the cross-system comparison.

Table 14. Cross-system comparison—IEEE 39-bus benchmark vs. NZ HVDC validation.

Parameter	IEEE 39-Bus	NZ HVDC (2024)
TTC (MW)	300	1050
Resolution/W_base	5 min/30 min	30 min/24 h
K bounds	[1.10, 2.50]	[1.10, 2.00]
γ (Equation (29))	0.5355	0.6018
σ_ref (MW)	112.68	126.29
σ_TTC max/min	24.09	25.36
Mean K(t)/saturation	1.632/11.1%	1.626/12.2%
ΔATC 2 $\rightarrow$ 3 (MW/%)	+78.11/+217.7%	+59.51/+7.6%
ΔATC 3 $\rightarrow$ 4 (MW/%)	Cs	$-6.74/-0.8\%$
TRM/TTC (Proposed)	56.9%	20.4%
Time constrained (%)	18.1%	0.0%

As renewable penetration and northward HVDC transfers increase, the NZ corridor is expected to operate more frequently in a congested regime, increasing the practical value of $K(t)$ scheduling. The recovered 59.51 MW of ATC translates directly into additional northward export capacity for South Island renewable generation. Full NZ results, including the four-way comparison and volatility, duration, and allocation profiles, are provided in Appendix A.

5.6. Risk and Reliability Validation

The proposed framework recovers transfer capacity by temporally redistributing reliability margin. This subsection verifies that the redistribution does not create systematic

under-protection by reporting the one-sided coverage, violation rate, and exceedance severity for both test systems.

Coverage is defined as $P_{\text{cov}} = \Pr\,(e(t) \leq \text{TRM}(t))$, evaluated against a one-sided 95% target. The violation rate is $P_{\text{viol}} = 1 - P_{\text{cov}}$, and exceedance severity is quantified by the conditional mean exceedance $\mathbb{E}[e(t) - \text{TRM}(t) \mid e(t) > \text{TRM}(t)]$, which captures the average breach magnitude beyond frequency. On the NZ dataset, one-step-ahead persistence yields heavier-tailed forecast errors than the Gaussian assumption implicit in $K_{\text{base}} = 1.645$, explaining the observed 2–3 percentage point coverage shortfall relative to the 95% target. Under an operational forecasting model with smaller and less heavy-tailed errors, coverage would be expected to move closer to 95%; alternatively, the baseline confidence factor can be increased (e.g., $K_{\text{base}} \approx 1.85$) without altering the framework structure. Table 15 reports the coverage and exceedance metrics for all four approaches.

Table 15. One-sided coverage and exceedance metrics.

Metric	1: Static (7.5%)	2: MCS (P95)	3: Fixed-K Rolling	4: Proposed Adaptive
IEEE 39-bus (analytical)				
Coverage (%)	57.8	98.9	95.0	93.9
Violation rate (%)	42.2	1.1	5.0	6.1
NZ HVDC (empirical)				
Coverage (%)	78.7	96.2	92.6	91.8
Violation rate (%)	21.3	3.8	7.4	8.2
Mean exceedance (MW)	107.4	81.5	63.3	57.8
Max exceedance (MW)	748.3	559.8	360.8	273.8

IEEE values are analytical under the local Gaussian assumption; NZ values are empirical from 17,518 valid operating intervals.

To assess seasonal consistency, the NZ dataset is partitioned into four quarters (Table 16). Rolling approaches exhibit stable coverage across seasons, with an inter-quarter standard deviation below 1.1 percentage points, indicating no pronounced seasonal bias.

Table 16. Quarterly one-sided coverage (NZ HVDC, %).

Approach	Q1	Q2	Q3	Q4	Std Dev
3: Fixed-K	93.5	91.5	92.3	93.2	0.89
4: Proposed	91.4	91.3	93.4	91.0	1.08

The 1–3 percentage point gap between the 95% target and the empirical coverage (93.9% IEEE, 91.8% NZ) is attributable primarily to the heavy-tailed residuals of the persistence-based baseline forecaster relative to the Gaussian assumption implicit in $K_{\text{base}} = 1.645$. On the NZ corridor, one-step-ahead persistence occasionally produces large forecast errors that exceed the Gaussian-calibrated margin. This reflects a limitation of the baseline forecaster rather than of the adaptive TRM structure itself: (i) under an operational forecasting model with smaller and less heavy-tailed residuals, coverage would be expected to move closer to 95%; (ii) K_{base} can be increased (e.g., to ≈ 1.85 for the NZ corridor) to recover empirical coverage without altering the framework structure; and (iii) the coverage remains seasonally stable (inter-quarter standard deviation < 1.1 percentage points, Table 16), confirming no pronounced temporal bias.

5.7. Computational Performance

Table 17 summarizes the execution times on a standard workstation (Intel Core i7-12700, 32 GB RAM, MATLAB R2024a). The computationally dominant stage is the AC power flow TTC evaluation, requiring ~63 s for 1000 scenarios on the IEEE 39-bus system. This is performed offline for probabilistic characterization (Section 5.2) and is not repeated at each dispatch interval. In contrast, the online component—rolling $\sigma_{\mathrm{TTC}}(t)$ estimation, adaptive window updates, $K(t)$ scheduling, and TRM/ATC calculation—runs in <10 ms per time step, which is negligible for 5–30 min dispatch cycles.

Table 17. Computational performance summary.

Stage	IEEE 39-Bus	NZ HVDC
LHS + Iman–Conover (N = 1000)	0.8 s	0.8 s
AC power flow per scenario	0.06 s	N/A
Full TTC evaluation (1000 × PF)	62.7 s	N/A
Rolling + K(t) per step	<0.01 s	<0.01 s
Full 24 h dynamic TRM (288 steps)	0.4 s	--
Full annual analysis (17,518 steps)	--	1.2 s

For the NZ annual validation, the rolling analysis over 17,566 half-hourly intervals completes in 1.2 s, indicating linear scaling and practical deployability. By comparison, recomputing an MCS-based *P*95 margin at every time step would take ~5 h for a single 24 h IEEE horizon, demonstrating that the rolling window method achieves comparable reliability (Section 5.5) at a small fraction of the computational cost.

5.8. Assumptions and Limitations

Firstly, forecast deviations use a persistence baseline (Equations (23) and (24)), providing a conservative reference. The framework is forecaster-agnostic: any realized residuals can be substituted into the rolling window estimator without altering uncertainty propagation or TRM scheduling, so benefits persist wherever volatility remains time-varying.

Secondly, injection-to-TTC sensitivity coefficients are obtained from a single variance decomposition snapshot (Section 5.2) and treated as time-invariant. In practice, these vary with the operating point and active constraint set. Periodic re-linearization would improve accuracy during constraint-switching transitions.

Thirdly, constraint-side uncertainty is limited to stochastic thermal capacity variability (Equations (19) and (20)); topology and contingencies are enforced deterministically. This does not capture dynamic line rating or probabilistic outage states. Section 5.2 shows thermal rating uncertainty is negligible once voltage limits bind, so reported gains are primarily injection-driven.

Finally, the New Zealand validation uses a single corridor with fixed TTC for comparability. Future work should incorporate time-varying TTC, multi-corridor meshed networks, and broader constraint-side modeling where such mechanisms are material.

6. Discussion

The proposed framework advances probabilistic ATC assessment by replacing static or pooled margins with a dynamic TRM that adapts to time-varying uncertainty. The rolling window mechanism is computationally lightweight (<10 ms per interval) and integrates into existing EMS workflows without altering dispatch architecture, unlike offline stochastic or distributionally robust formulations.

Two structural insights emerge. Firstly, volatility tracking is the dominant capacity recovery driver: across both case studies, most ATC gains arise from replacing pooled margins with rolling estimates, indicating substantial benefit before introducing confidence scheduling. Secondly, α-based scheduling is regime-dependent—additional headroom arises on congested interfaces with frequent binding constraints, while uncongested corridors show limited incremental benefit. As penetration grows and interfaces operate closer to limits, the value of adaptive scheduling is expected to increase.

Cross-system results (Table 14) confirm consistent non-stationarity across substantially different contexts, supporting generalizability. Correlation-aware propagation is operationally material: neglecting dependence understates lower-tail TTC and biases TRM downward during stress conditions. Reliability validation on New Zealand data shows stable coverage; shortfalls are attributable to heavy-tailed persistence errors rather than structural limitations.

The recovered ATC (93.31 MW on IEEE; 59.51 MW on the NZ HVDC link) translates directly into export headroom that static margins would otherwise withhold, linking dynamic transmission margining to curtailment reduction at the transmission–distribution interface. The framework extends our earlier formulation by incorporating solar uncertainty, stochastic constraint variability, correlation-aware scenario generation, and cross-system validation.

From a scalability perspective, the proposed framework separates naturally into offline and online stages with distinct growth characteristics. The offline stage—LHS scenario generation and AC power flow evaluation—scales with network size and scenario count; for the IEEE 39-bus system, 1000 scenarios require about 63 s (Table 17). For larger networks, the per-scenario AC power flow cost increases, but the required LHS sample count need not grow proportionally with network size because the dominant uncertain inputs typically remain modest relative to the total network dimension. By contrast, the online stage—rolling window estimation of $\sigma_{\mathrm{TTC}}(t)$, adaptive window updates, confidence factor scheduling, and TRM/ATC computation—is independent of network size and executes in under 10 ms per time step (Table 17), making it suitable for real-time deployment. In meshed multi-corridor systems, the framework can be applied independently to each monitored interface, with the online computations parallelizable across corridors.

7. Conclusions

This paper developed a probabilistic ATC framework in which TRM is updated dynamically via rolling window uncertainty tracking and adaptive confidence factor scheduling, addressing static margins that cannot follow time-varying uncertainty and constant probabilistic margins anchored to worst-case statistics.

Key findings from the IEEE 39-bus benchmark and New Zealand HVDC corridor validation:

(1) Scenario efficiency: LHS with Iman–Conover correlation control matched a 10,000-sample MCS baseline using 1000 scenarios (mean TTC deviation $\leq 0.13\%$, $8.6\times$ speed-up). Correlation control shifted the 5th-percentile TTC by 23.35 MW, confirming that independent sampling understates downside risk.

(2) Dominant uncertainty source: Renewable uncertainty dominated TTC variability (96.7% of variance); thermal rating uncertainty contributed ~0%, indicating injection-side uncertainty drives dynamic TRM in the studied regime.

(3) Volatility tracking drives capacity recovery: The adaptive estimator captured strong non-stationarity (max/min σ: 24.09 IEEE; 25.36 NZ), recovering 78.11 MW and 59.51 MW mean ATC respectively—establishing volatility tracking as the primary recovery mechanism.

(4) Regime dependence of α: α scheduling yielded +15.20 MW (+13.3%) on the congested IEEE corridor (TRM/TTC = 56.9%) but no gain on the uncongested NZ corridor (TRM/TTC = 20.4%), indicating the greatest value on constrained interfaces.
(5) Reliability: Rolling policies achieved ~92–95% one-sided coverage, stable across seasons (inter-quarter std < 1.1%), with per-interval computation < 10 ms.
(6) Renewable export headroom: Recovered capacity (93.31 MW IEEE; 59.51 MW NZ) translates directly into additional export headroom at the transmission–distribution interface, reducing curtailment without compromising security.

A supplementary scalability check on the IEEE 118-bus system (Appendix B) confirms that the adaptive update mechanism remains computationally lightweight and operationally active on a larger network.

Future work will extend to multi-corridor meshed networks, time-varying TTC, and interactions with flexibility resources and distribution network modeling. As congestion increases, the value of α scheduling is expected to grow.

Author Contributions: Conceptualization, U.E.E., T.T.L. and M.A.M.; Methodology, U.E.E. and T.T.L.; Software, U.E.E.; Validation, U.E.E.; Formal analysis, U.E.E.; Investigation, U.E.E.; Data curation, U.E.E.; Writing—original draft, U.E.E.; Writing—review & editing, U.E.E., T.T.L. and M.A.M.; Visualization, T.T.L. and M.A.M.; Supervision, T.T.L. and M.A.M. All authors have read and agreed to the published version of the manuscript.

Funding: This research received no external funding.

Data Availability Statement: The original contributions presented in this study are included in the article. Further inquiries can be directed to the corresponding author.

Conflicts of Interest: The authors declare no conflict of interest.

Appendix A. Detailed New Zealand HVDC Corridor Validation

This appendix provides the detailed results for the New Zealand HVDC inter-island corridor validation summarized in Section 5.5. The four-way TRM/ATC comparison (Table A1) uses half-hourly EMI operational data from January–December 2024 (17,566 samples). Forecast errors are computed using one-step-ahead persistence, and the transfer corridor is modeled with fixed TTC = 1050. Rolling window parameters are $W_{\text{base}} = 48$ samples (24 h), $W_{\min} = 12$ (6 h), and $W_{\max} = 336$ (7 days), with $K(t)$ bounded to [1.10, 2.00].

Table A1. Four-way TRM/ATC comparison—NZ HVDC corridor (TTC = 1050 MW).

Metric	1: Static (7.5%)	2: MCS (P95 TRM)	3: Fixed-K Rolling	4: Proposed Adaptive
Mean TRM (MW)	78.75	267.25	207.75	214.48
Mean ATC (MW)	971.25	782.75	842.25	835.52
TRM as % of TTC	7.5%	25.5%	19.8%	20.4%
Adaptation ratio	1.0:1	1.0:1	25.4:1	46.1:1

The rolling window transition (Approach 2 → 3) recovers +59.51 MW of the mean ATC (+7.6%). The $K(t)$ scheduling layer behaves as designed—mean $K(t) = 1.626$ (≈1.2% below K_{base}), saturation frequency 12.2%, and TRM dynamic range 46.1:1—yet yields only a +6.74 MW marginal TRM increase (−0.8% ATC change). This outcome is explained by the NZ corridor congestion regime: TRM/TTC = 20.4% and the ATC floor constraint never activates (0% binding). Consequently, the positive dependence between $K(t)$ and

$\sigma(t)$ implied by Equation (28) is fully realized, increasing $\mathbb{E}[K(t)\sigma(t)]$ relative to fixed-K scaling. This contrasts with the IEEE corridor, where 18.1% binding introduces truncation asymmetry that enables scheduling to reduce the mean TRM.

Figure A1 shows the rolling volatility $\sigma_{\mathrm{TTC}}(t)$ profile, confirming strong non-stationarity with seasonal patterns driven by weather-dependent wind variability. Figure A2 presents the ATC duration curves: rolling approaches dominate the MCS policy across most percentiles, whereas the static rule yields the highest nominal ATC without probabilistic protection. Figure A3 illustrates the stacked TRM/ATC allocation, visually confirming the low congestion level (TRM/TTC = 20.4%) relative to the IEEE benchmark.

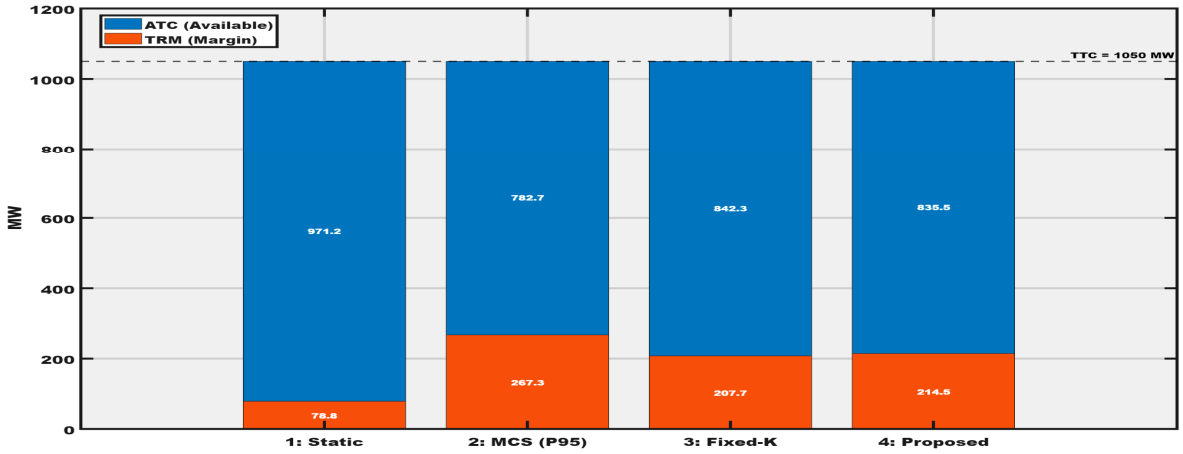

Figure A1. Rolling volatility σTTC(t) profile for the NZ HVDC corridor over 24 h.

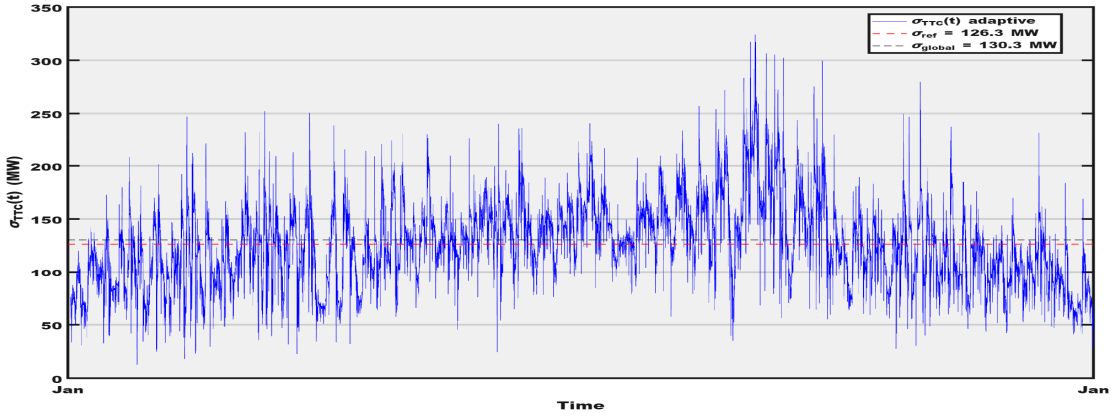

Figure A2. ATC duration curves for all four benchmark approaches on the NZ HVDC corridor.

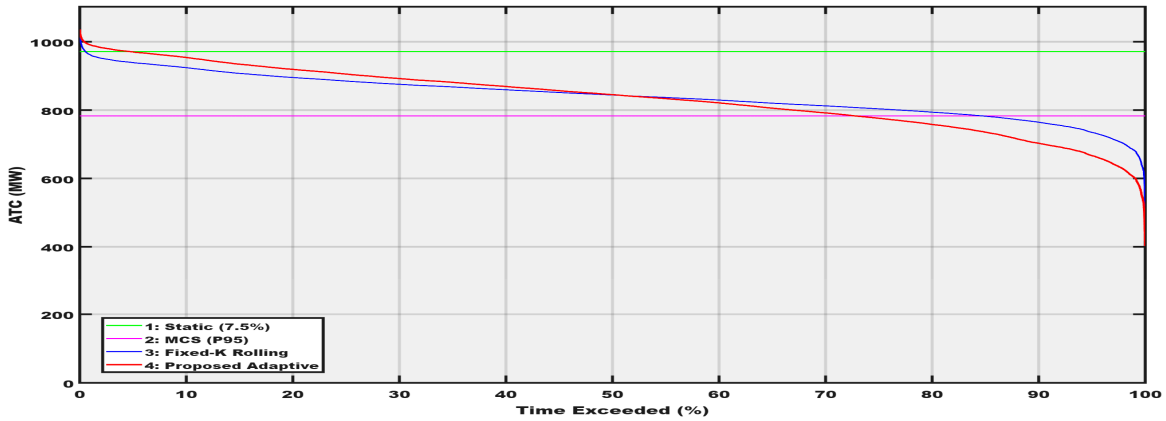

Figure A3. Stacked TRM/ATC allocation for the NZ HVDC corridor.

Appendix B. Supplementary IEEE 118-Bus Scalability Check

To provide a supplementary indication of scalability, the proposed adaptive TRM update mechanism was applied to the IEEE 118-bus system. This experiment is intended as a computational scalability check rather than as a full validation case equivalent to the IEEE 39-bus and New Zealand studies. In particular, TTC is approximated from the aggregate thermal ratings of the monitored tie-lines, and the test is used primarily to assess whether the adaptive update mechanism remains computationally lightweight and operationally active on a larger network.

The IEEE 118-bus system was partitioned into two areas, buses 1–69 and 70–118, connected by 12 inter-area tie-lines, yielding an approximate TTC of 1350 MW. A 24 h synthetic non-stationary forecast error trajectory with 5 min resolution was used, giving 241 valid online update steps after initialization. The adaptive TRM parameters were retained from the main framework, with $K(t)$ constrained to [1.10, 2.50].

Table A2 summarizes the results. The adaptive mechanism remains fully active on the larger network, with $K(t)$ spanning the full prescribed range [1.10, 2.50] and a mean value of 1.801. The resulting mean TRM is 304.45 MW, corresponding to 22.6% of TTC, while the mean ATC is 1045.55 MW. The TRM varies between 51.58 MW and 739.39 MW, giving an adaptation ratio of 14.3:1 and confirming substantial temporal flexibility in the margin assignment.

For reference, the static 7.5% margin yields a TRM of 101.25 MW, while the one-sided empirical P_{95} baseline gives 304.51 MW. The proposed adaptive method achieves one-sided coverage of 83.0%, compared with 66.0% for the static margin and 95.0% for the empirical P_{95} baseline. Although this coverage is lower than that reported for the main IEEE 39-bus study, it remains within the broad range observed in earlier larger-network scalability experiments and should be interpreted considering the approximate corridor definition and the absence of full AC probabilistic TTC recalibration in this appendix test.

Most importantly, the online computational burden remains negligible. The full online stage requires only 8.31 ms for the 24 h trajectory, corresponding to 0.0345 ms per time step. This confirms that the adaptive TRM update mechanism remains suitable for real-time deployment even when transferred to a substantially larger network.

Table A2. IEEE 118-bus scalability comparison.

Metric	IEEE 39-Bus (Section 5)	IEEE 118-Bus (Appendix B)
Network size (buses)	39	118
TTC (MW)	300	1350
Mean TRM (MW)	170.81	304.45
Mean ATC (MW)	129.19	1045.55
TRM/TTC (%)	56.9	22.6
Adaptation ratio	19.1:1	14.3:1
Mean K(t)	1.632	1.801
One-sided coverage (%)	93.9	83.0
Online time per step (ms)	<0.01 s	1.2 s

References

1. Holttinen, H.; Groom, A.; Kennedy, E.; Woodfin, D.; Barroso, L.; Orths, A.; Ogimoto, K.; Wang, C.; Moreno, R.; Parks, K.; et al. Variable renewable energy integration: Status around the world. *IEEE Power Energy Mag.* **2021**, *19*, 86–96. [CrossRef]

2. North American Electric Reliability Council. *Available Transfer Capability Definitions and Determination*; Technical Report; North American Electric Reliability Council: Princeton, NJ, USA, 1996. Available online: https://www.ece.iit.edu/ flueck/ece562/atcfinal.pdf (accessed on 5 March 2026).
3. Shin, D.-J.; Kim, J.-O.; Kim, K.-H.; Singh, C. Probabilistic approach to available transfer capability calculation. *Electr. Power Syst. Res.* **2007**, *77*, 813–820. [CrossRef]
4. Mohammed, O.O.; Mustafa, M.W.; Mohammed, D.S.S.; Otuoze, A.O. Available transfer capability calculation methods: A comprehensive review. *Int. Trans. Electr. Energy Syst.* **2019**, *29*, e2846. [CrossRef]
5. Roald, L.; Oldewurtel, F.; Van Parys, B.; Andersson, G. Security constrained optimal power flow with distributionally robust chance constraints. *arXiv* **2015**, arXiv:1508.06061. [CrossRef]
6. Reyad, H.W.; Elfar, M.; El-Araby, E.E. Probabilistic Assessment of Available Transfer Capability Incorporating Load and Wind Power Uncertainties. *IEEE Access* **2023**, *11*, 39048–39065. [CrossRef]
7. Meng, X.; Zhang, L.; Tian, X.; Chu, H.; Wang, Y.; Shi, Q. Available transfer capability assessment of multiarea power systems with conditional generative adversarial network. *Int. Trans. Electr. Energy Syst.* **2024**, *2024*, 5225784. [CrossRef]
8. Wei, C.; Jia, L.; Wang, X.; Cai, Y.; Huang, Y.; Huang, Y.; Liao, S. Calculation of the available transfer capability of trading channels based on power network congestion forecasting. *Front. Energy Res.* **2024**, *12*, 1351306. [CrossRef]
9. Li, W.; Vaahedi, E.; Lin, Z. BC Hydro's transmission reliability margin assessment in total transfer capability calculations. *IEEE Trans. Power Syst.* **2013**, *28*, 4796–4802. [CrossRef]
10. Edeh, U.E.; Lie, T.T.; Mahmud, M.A. Assessment of Transmission Reliability Margin: Existing Methods and Challenges and Future Prospects. *Energies* **2025**, *18*, 2267. [CrossRef]
11. Sun, X.; Tian, Z.; Rao, Y.; Li, Z.; Tricoli, P. Probabilistic available transfer capability assessment in power systems with wind power integration. *IET Renew. Power Gener.* **2020**, *14*, 1912–1920. [CrossRef]
12. Li, Q.; Wang, X.; Rong, S. Probabilistic Load Flow Method Based on Modified Latin Hypercube-Important Sampling. *Energies* **2018**, *11*, 3171. [CrossRef]
13. Karimi, S.; Musilek, P.; Knight, A.M. Dynamic thermal rating of transmission lines: A review. *Renew. Sustain. Energy Rev.* **2018**, *91*, 600–612. [CrossRef]
14. Edeh, U.E.; Lie, T.T.; Mahmud, M.A. Dynamic TRM Estimation with Load–Wind Uncertainty Using Rolling Window Statistical Analysis for Improved ATC. *Energies* **2026**, *19*, 844. [CrossRef]
15. Hajian, M.; Rosehart, W.D.; Zareipour, H. Probabilistic power flow by Monte Carlo simulation with Latin supercube sampling. *IEEE Trans. Power Syst.* **2012**, *28*, 1550–1559. [CrossRef]
16. Yu, H.; Chung, C.; Wong, K.; Lee, H.; Zhang, J. Probabilistic load flow evaluation with hybrid latin hypercube sampling and Cholesky decomposition. *IEEE Trans. Power Syst.* **2009**, *24*, 661–667. [CrossRef]
17. Roald, L.A.; Pozo, D.; Papavasiliou, A.; Molzahn, D.K.; Kazempour, J.; Conejo, A. Power systems optimization under uncertainty: A review of methods and applications. *Electr. Power Syst. Res.* **2023**, *214*, 108725. [CrossRef]
18. Ejebe, G.C.; Tong, J.; Waight, J.G.; Frame, J.G.; Wang, X.; Tinney, W.F. Available transfer capability calculations. *IEEE Trans. Power Syst.* **1998**, *13*, 1521–1527. [CrossRef]
19. Zimmerman, R.D.; Murillo-Sánchez, C.E.; Thomas, R.J. MATPOWER: Steady-state operations, planning, and analysis tools for power systems research and education. *IEEE Trans. Power Syst.* **2010**, *26*, 12–19. [CrossRef]
20. Shao, D.; Li, H.; Li, J.; Yu, X.; Sun, X.; Han, B. Uncertainty modeling method for wind and solar power output in building integrated energy systems under continuous anomalous weather. *arXiv* **2025**, arXiv:2504.11100. [CrossRef]
21. Fernandez-Jimenez, L.A.; Monteiro, C.; Ramirez-Rosado, I.J. Short-term probabilistic forecasting models using Beta distributions for photovoltaic plants. *Energy Rep.* **2023**, *9*, 495–502. [CrossRef]
22. Atwa, Y.M.; El-Saadany, E.; Salama, M.; Seethapathy, R. Optimal renewable resources mix for distribution system energy loss minimization. *IEEE Trans. Power Syst.* **2009**, *25*, 360–370. [CrossRef]
23. Kundur, P. Power system stability. In *Power System Stability and Control*; Grigsby, L.L., Ed.; CRC Press: Boca Raton, FL, USA, 2007; Chapter 7, pp. 7-1–7-12, ISBN 978-0-8493-9291-7.
24. Rashkovska, A.; Jančič, M.; Depolli, M.; Kosmač, J.; Kosec, G. Uncertainty Assessment of Dynamic Thermal Line Rating for Operational Use at Transmission System Operators. *IEEE Trans. Power Syst.* **2022**, *37*, 4642–4650. [CrossRef]
25. Iman, R.L.; Conover, W.-J. A distribution-free approach to inducing rank correlation among input variables. *Commun. Stat.-Simul. Comput.* **1982**, *11*, 311–334. [CrossRef]
26. Edeh, U.E.; Lie, T.; Mahmud, M.A. Dynamic Transmission Reliability Margin Assessment Using Rolling Window Statistical Analysis for Enhanced Available Transfer Capability. In *Proceedings of the 2025 IEEE Region 10 Symposium (TENSYMP), Christchurch, New Zealand, 10 July 2025*; IEEE: New York, NY, USA, 2025; pp. 1–6.
27. Papaefthymiou, G.; Kurowicka, D. Using Copulas for Modeling Stochastic Dependence in Power System Uncertainty Analysis. *IEEE Trans. Power Syst.* **2009**, *24*, 40–49. [CrossRef]

28. Sheng, H.; Wang, X. Probabilistic Power Flow Calculation Using Non-Intrusive Low-Rank Approximation Method. *IEEE Trans. Power Syst.* **2019**, *34*, 3014–3025. [CrossRef]
29. Douglass, D.A.; Edris, A.-A. Real-time monitoring and dynamic thermal rating of power transmission circuits. *IEEE Trans. Power Deliv.* **2002**, *11*, 1407–1418. [CrossRef]
30. Electricity Authority New Zealand. Electricity Market Information (EMI) Datasets. Available online: https://www.emi.ea.govt.nz/Wholesale/Datasets/Generation/Generation_MD (accessed on 6 January 2026).
31. Transpower New Zealand. Examining the Purpose and Future Role of Our HVDC Link. Wellington, Discussion Paper March 2024. 2024. Available online: https://www.transpower.co.nz/about-us/our-strategy/discussion-papers (accessed on 18 February 2026).